



Effects of Hydrogen Enrichment on Thermoacoustic and Helical Instabilities in Swirl Stabilised Partially Premixed Flames

Ankit D. Kumar¹ · James C. Massey^{1,2} · Isaac Boxx^{3,4} · Nedunchezian Swaminathan¹

Received: 29 April 2023 / Accepted: 6 October 2023
© The Author(s) 2023

Abstract

The effects of hydrogen enrichment on flame and flow dynamics of a swirl-stabilised partially premixed methane-air flame are studied using large eddy simulation. The sub-grid reaction rate is modelled using unstrained premixed flamelets and a presumed joint probability density function approach. Two cases undergoing thermoacoustic oscillations at ambient conditions are studied. The addition of hydrogen modifies both thermoacoustic and fluid dynamical characteristics. The amplitude of the fundamental thermoacoustic mode increases with the addition of 20% hydrogen by volume. A second pressure mode associated with the chamber mode is also excited with the hydrogen addition. Intermittent single, double and triple helical instabilities are observed in the pure methane case, but are suppressed substantially with hydrogen addition. The results are analysed in detail to shed light on these observations. The feedback loop responsible for the thermoacoustic instability is driven by mixture fraction perturbations resulting from the unequal impedances of the fuel and air channels. It is shown that hydrogen addition increases the flame's sensitivity to these perturbations, resulting in an increase in amplitude. This higher amplitude thermoacoustic oscillation, along with a higher local heat release rate in the presence of hydrogen, is shown to considerably modify the flow structures, leading to a suppression of the helical instabilities.

Keywords Hydrogen combustion · Large eddy simulation · Thermoacoustic oscillation · Swirling flame · Helical instabilities

1 Introduction

The increasing demand for green energy necessitates the development of low-cost novel technology and hydrogen as an energy carrier has the potential to tackle the energy storage problem of intermittent renewable sources (Yue et al. 2021). Retrofitting the current Gas Turbine (GT) with technology for using hydrogen-enriched fuels promises a significant reduction in greenhouse gas emissions (Nemitallah et al. 2018), which also addresses grid-level storage issues encountered by intermittent renewable sources. Therefore, there is

Extended author information available on the last page of the article

a growing interest in comprehending the dynamics of swirl-stabilized hydrogen flames for aeronautical and ground-based GT combustors.

Several past studies (Yu et al. 1986; Gauducheau et al. 1998; Schuller et al. 2022; Aniello et al. 2023; Chtereve and Boxx 2021; Indlekofer et al. 2021) have provided useful insights on hydrogen-enriched methane-air flames. These studies demonstrated that hydrogen-enriched fuels exhibit larger laminar flame speeds and extinction strain rates. Consequently, hydrogen-enriched flames have improved blow-off characteristics, but are more susceptible to flame flashback (Tuncer et al. 2009). Practical combustors typically operate under partially premixed conditions to prevent flame flashback. However, the partial premixing preventing the flashback may result in thermoacoustic instabilities (TAI) caused by equivalence ratio fluctuations (Lieuwen and Zinn 1998; Ducruix et al. 2003). Combustors typically operate under lean conditions to meet stringent emission regulations for NO_x emissions, making them susceptible to TAI (Dowling and Hubbard 2000). Long-term operation of GT combustors under unstable conditions can lead to fatigue induced structural damage. Therefore, stable operation with no self-excited TAI is essential for low-cost operation of GT combustors. Understanding the effects of hydrogen enrichment on TAI is important for decarbonisation.

Hydrogen combustion results in several changes in combustion characteristics. For instance, hydrogen enrichment leads to a change in the mean flame length altering the convective time scales for velocity and equivalence ratio fluctuations (Beita et al. 2021). This change in the convective time scale of fluctuations in heat release can alter the frequency of thermoacoustic instability (Ghani and Polifke 2021). The change in flame length can also lead to mode switching to higher harmonics (Lee et al. 2015). Also, the change in flame shape resulting from higher extinction strain rates seems to excite TAI in some hydrogen-enriched turbulent flames as observed in Shanbhogue et al. (2016). Hence, the influences of H_2 enrichment on turbulent flow with partially premixed combustion and TAI are investigated in this study.

The addition of hydrogen leads to complex non-linear dynamical states in combustion systems. For instance, hydrogen enrichment showed an intermittency route (Kabiraj and Sujith 2012) to limit cycle oscillation (LCO) in a swirl-stabilized combustor (Karlis et al. 2019). Recent studies have investigated the influence of hydrogen addition on flame topology, combustion characteristics, and bimodal thermoacoustic instability (Chtereve and Boxx 2019; Agostinelli et al. 2022). Various dynamical states such as intermittency, period-1 LCO, period-2 LCO, and chaotic state were observed for hydrogen-enriched flames in the PRECCINSTA burner (Kushwaha et al. 2021). Period-1 LCO was the focus of previous experimental and numerical studies using the PRECCINSTA burner (Meier et al. 2007; Franzelli et al. 2012; Lourier et al. 2017; Stöhr et al. 2017; Fredrich et al. 2021a, b). Here, the effects of hydrogen enrichment on the transition from period-1 to period-2 LCO behavior are studied.

Swirl is commonly used for flame stabilisation in GT combustors (Syred 2006; Lucca-Negro and O'doherty 2001). Above a critical swirl number, which depends on the geometry and flow conditions, the vortex breakdown bubble (VBB) precesses about the central axis as a result of super-critical Hopf bifurcation (Liang and Maxworthy 2005; Manoharan et al. 2020). This results in the formation of precessing vortex core (PVC) which plays a crucial role in flame stabilisation and mixing (Gupta et al. 1984; Syred 2006; Meier et al. 2006; Weigand et al. 2006; Massey et al. 2019, 2022). The PVC in reacting flows may be severely damped (Syred 2006; Roux et al. 2005), occur intermittently (Oberleithner et al. 2015; Fredrich et al. 2021b; Yin and Stöhr 2020) or is sustained fully (Chen et al. 2019a; Massey et al. 2019; Karmarkar et al. 2022) depending on the flow and thermo-chemical

conditions. Viscous damping (Roux et al. 2005), centrifugal stability (Syred 2006; Rayleigh 1917) or density stratification along with backflow intensity (Terhaar et al. 2015; Oberleithner et al. 2015) can suppress the PVC under reacting conditions. While transient PVC dynamics have been studied extensively in the PRECCINSTA burner (Yin and Stöhr 2020; Oberleithner et al. 2015; Zhang et al. 2023) for premixed cases, this work attempts to capture such dynamics in partially premixed cases using LES. The linear stability analysis of Oberleithner et al. (2015) showed that the higher density stratification in cases with global equivalence ratio $\phi_{\text{glob}} > 0.65$ at a thermal load of $P_{\text{th}} = 20\text{kW}$ were correlated with the lower PVC growth rates. Zhang et al. (2023) have quantitatively shown the competition between convection, production and viscous diffusion of velocity perturbation to play an important role in intermittent PVC dynamics. The PVC is often denoted as a helical instability with an azimuthal wavenumber $m = 1$ of fluctuating velocity component. Recent studies have shown the presence of higher azimuthal wavenumbers in reacting flows (Vignat et al. 2021) similar to those found under non-reacting conditions (Liang and Maxworthy 2005; Vanierschot et al. 2018). The thermoacoustic oscillation can modulate the PVC (Chen et al. 2019a) and even suppress it intermittently in some cases (Vignat et al. 2021). Thus it is useful to study the effects of H_2 addition on the PVC.

The foregoing discussion identifies the following objectives:

1. To investigate the effects of H_2 -addition on the flame, flow and TAI characteristics,
2. Specifically of the transition from period-1 to period-2 LCO, and
3. Changes in the structure and role of PVC because of H_2 -enrichment. These objectives are addressed by conducting LES of H_2 -enriched combustion in PRECCINSTA burner. A presumed joint probability density function approach (PDF) with tabulated chemistry is used to model the filtered reaction rate (Ruan et al. 2014; Chen et al. 2017, 2019a, b, 2020; Chen and Swaminathan 2020; Langella et al. 2018, 2020; Massey et al. 2022; Fiorina et al. 2003).

This paper is organised as follows. The modelling methodology is described in Sect. 2. The cases studied and their numerical setup are presented in Sect. 3. The details of the non-reacting flow field, comparisons of LES with measurements along with grid-dependency are discussed in Sect. 4.1. The comparisons of LES statistics to measurements and reacting flow structure are presented in Sect. 4.2. The thermoacoustic instability mechanisms are discussed in Sect. 4.3. The interactions of the coherent structures with the thermoacoustic oscillation are presented in Sect. 4.4 and a summary of the key findings is given in the final section.

2 Modelling Methodology

Fully compressible Favre-filtered transport equations for mass, momentum, and total enthalpy are solved. A presumed joint probability density function (PDF) approach with tabulated chemistry is used for sub-grid reaction rate closure (Ruan et al. 2014; Chen et al. 2017, 2019a, b, 2020; Chen and Swaminathan 2020; Langella et al. 2018, 2020; Massey et al. 2022; Fiorina et al. 2003). The adiabatic flamelet library is obtained using Cantera (v2.4.0) (Goodwin et al. 2018) which solves the steady one-dimensional freely propagating flame equations for species transport and temperature. The flamelet equations are solved with a multicomponent transport model. The mixture fraction, which tracks fuel-air

mixing, is calculated using Bilger's formula (Bilger 1989). The progress variable is a measure of the reaction extent and defined as $c \equiv \psi/\psi^{\text{eq}}$, where $\psi \equiv Y_{\text{CO}} + Y_{\text{CO}_2}$, and ψ^{eq} represents the equilibrium value for the local mixture (Fiorina et al. 2003). Thermochemical quantities are functions of mixture fraction $\tilde{\xi}$, \tilde{c} , and their respective sub-grid scale (SGS) variances. These 4 quantities and the total enthalpy are obtained from their transport equations (Chen et al. 2017; Massey et al. 2021), written as

$$\frac{\overline{D\tilde{\varphi}}}{Dt} = \nabla \cdot (\overline{\rho D_{\text{eff}} \nabla \tilde{\varphi}}) + \overline{S_{\varphi}^+} - \overline{S_{\varphi}^-}, \quad (1)$$

where the vectors of Favre-filtered scalars, source and sink terms are respectively given by

$$\tilde{\varphi} = \left\{ \tilde{\xi}, \sigma_{\xi, \text{sgs}}^2, \tilde{c}, \sigma_{c, \text{sgs}}^2, \tilde{h} \right\}, \quad (2)$$

$$\overline{S_{\varphi}^+} = \left\{ 0, 2 \frac{\mu}{Sc_t} |\nabla \tilde{\xi}|^2, \overline{\dot{\omega}_c^*}, 2 \frac{\mu}{Sc_t} |\nabla \tilde{c}|^2 + 2(c\overline{\dot{\omega}_c^*} - \tilde{c}\overline{\dot{\omega}_c^*}), \frac{D\overline{p}}{Dt} \right\}, \quad (3)$$

$$\overline{S_{\varphi}^-} = \{0, 2\overline{\rho} \tilde{\chi}_{\xi, \text{sgs}}, 0, 2\overline{\rho} \tilde{\chi}_{c, \text{sgs}}, 0\}. \quad (4)$$

The effective diffusivity is $D_{\text{eff}} = D + \nu_t/Pr_t$ with $Pr_t = 0.7$ for total enthalpy and Pr_t is replaced by Sc_t for other scalars with $Sc_t = 0.7$. The values for the turbulent Prandtl and Schmidt number are guided by past work (Chen et al. 2020; Langella et al. 2020; Kumar et al. 2023). The sub-grid eddy viscosity is ν_t and $\tilde{\chi}_{i, \text{sgs}}$ denotes the scalar dissipation rate of scalar i at the sub-grid level. The sub-grid eddy viscosity ν_t is modelled using the dynamic Smagorinsky model (Germano et al. 1991; Lilly 1992).

The flamelet reaction rate is $\dot{\omega}_{\text{fp}} = (\dot{\omega}_{\text{CO}} + \dot{\omega}_{\text{CO}_2})/\psi^{\text{eq}}$. A sub-grid model accounting for both premixed and non-premixed combustion modes is used and this model is Chen et al. (2017), Massey et al. (2021)

$$\begin{aligned} \overline{\dot{\omega}_c} &= \overline{\dot{\omega}_{\text{fp}}} + \overline{\dot{\omega}_{\text{np}}} = \overline{\rho} \int_0^1 \int_0^1 \frac{\dot{\omega}_{\text{fp}}(\eta, \zeta)}{\rho(\eta, \zeta)} \tilde{P}(\eta, \zeta) d\eta d\zeta \\ &+ \tilde{c} \left(\frac{\overline{\mu}}{Sc} |\nabla \tilde{\xi}|^2 + \overline{\rho} \tilde{\chi}_{\xi, \text{sgs}} \right) \\ &\times \int_0^1 \frac{1}{\psi^{\text{eq}}} \frac{d^2 \psi^{\text{eq}}}{d\xi^2} \tilde{P}_{\beta}(\eta) d\eta, \end{aligned} \quad (5)$$

where η and ζ are the sample space variables for ξ and c respectively. The joint Favre filtered density function is approximated as $\tilde{P}(\eta, \zeta) \approx \tilde{P}_{\beta}(\eta; \tilde{\xi}, \sigma_{\xi, \text{sgs}}^2) \times \tilde{P}_{\beta}(\zeta; \tilde{c}, \sigma_{c, \text{sgs}}^2)$, where the marginal filtered density functions are modelled using Beta functions. The sub-grid scalar dissipation rate, $\tilde{\chi}_{c, \text{sgs}}$ (Dunstan et al. 2013) is modelled using an algebraic model with the scale-dependent parameter β_c set to 7.5 following earlier studies (Ruan et al. 2014; Chen et al. 2017, 2019a, b, 2020; Chen and Swaminathan 2020; Langella et al. 2018, 2020; Massey et al. 2022). A linear relaxation model is used for the mixture fraction sub-grid scalar dissipation rate $\tilde{\chi}_{\xi, \text{sgs}}$ (Pierce and Moin 1998).

Thermochemical quantities such as specific heat capacity at constant pressure (\tilde{c}_p), molecular mass \tilde{M} and formation enthalpy $\tilde{\Delta h}_f^o$ of the mixture are computed analogous to Eq. (5). The mixture filtered density is obtained using $\overline{\rho} = \overline{p} \tilde{M} / (\tilde{T} \mathcal{R}_o)$, where $\mathcal{R}_o = 8.314 \text{ J mol}^{-1} \text{ K}^{-1}$ is the universal gas constant and \tilde{T} is the mixture filtered temperature. The

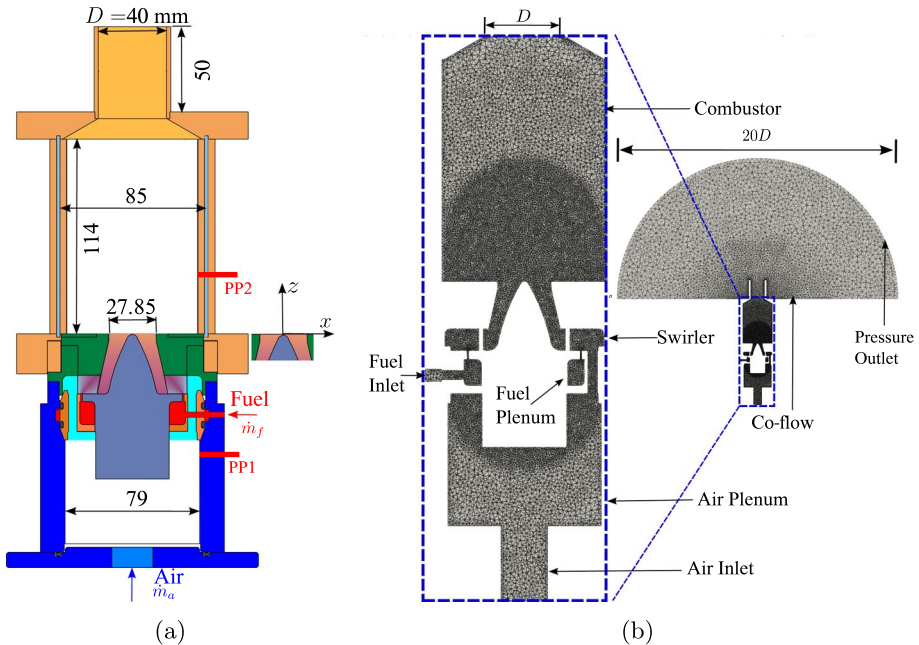


Fig. 1 **a** Schematic of the gas turbine model combustor (Meier et al. 2007; Dem et al. 2015) showing locations of pressure probe PP1 (LES) and PP2 (LES, Exp) and **b** part of the computational grid

solution of Eq. (1) gives control variables $\tilde{\xi}$, $\sigma_{\xi,sgs}^2$, \tilde{c} and $\sigma_{c,sgs}^2$ which are used to obtain various sources and thermo-chemical quantities from a lookup table. This modelling framework has been assessed for LES in Ruan et al. (2014), Chen et al. (2017, 2019a, b, 2020), Chen and Swaminathan (2020), Langella et al. (2018, 2020), Massey et al. (2022).

3 Experimental Case and Numerical Setup

Figure 1a shows the schematic of the PRECCINSTA (Meier et al. 2007; Dem et al. 2015) combustor. Dry air at ambient conditions enters the burner nozzle through 12 swirler vanes after passing through a plenum. Fuel is delivered to the fuel plenum through a channel below the swirler (Dem et al. 2015), in which the fuel is supplied through three ports leading to the fuel plenum. Two of the fuel inlet ports were closed off to test the influence of a single fuel inlet port on the thermoacoustic aspects, but no significant effect is observed. Therefore, the results in the rest of the paper correspond to three fuel inlets. The fuel plenum is included, as a previous study showed that it can play an important role in capturing the thermoacoustic behavior (Chen and Swaminathan 2020). This plenum feeds fuel into the air stream through 12 small holes located near the base of the swirler vanes. The conical central body in the convergent nozzle with exit diameter of 27.85 mm has its tip located at the nozzle exit plane (dump-plane). The PIV measurements are limited to a region bounded by $0 < z < 50$ mm and $-30 < x < 30$ mm. Further details of the experimental setup can be found in Datta et al. (2022), Kushwaha et al. (2021). The operating conditions are listed in Table 1.

Table 1 Summary of conditions simulated

Case	ϕ_{glob}	\dot{m}_f (g/s)	\dot{m}_a (g/s)	% H ₂ (vol.)	P_{th} (kW)
H0	0.65	0.40	10.55	0	20
H20	0.65	0.38	10.43	20	20
NR	–	–	10.55	–	–

The computational grid shown in Fig. 1b comprises of 8 million unstructured tetrahedral cells with a refinement in the swirler region and combustion zone (cell size of 0.8 mm). The hemispherical domain cells have an average size of 12 mm, while the remaining regions have a cell size of 1.5 mm. A finer grid is necessary for the swirler to resolve its geometry and to capture the subsequent flow development. A hemispherical domain is included to mimic the room volume. A small velocity of 0.1 m/s is specified at the base of this hemispherical domain, with a wave transmissive boundary condition on its outer boundary. Top-hat profiles of constant mass flow rates listed in Table 1 are specified without turbulence at the inlets. All walls are adiabatic with no-slip conditions, and Spalding's wall function is used for near-wall turbulence (Spalding 1960).

Temperature measurements are not available for the cases considered in this study. As an alternative to adiabatic boundary conditions, one of the three approaches summarised in Kraus et al. (2018) may be considered for treating the thermal boundary condition. The first option is to impose a guessed temperature profile to account for heat loss, which can lead to incorrect flame anchoring and an artificial forcing of the solution (Kraus et al. 2018). It was also observed (Gong 2022) that imposing an isothermal boundary condition led to extremely high thermoacoustic amplitudes which significantly moderate the flow field. Therefore, it is considered to be an undesirable option. The second option is to link the local wall temperature and heat flux, but this requires several LES runs to tune the heat resistance in the absence of temperature measurements. Finally, a coupled LES with conjugate heat transfer may be performed, fully accounting for the heat loss via conduction through the walls. Although this approach has the highest fidelity, the computational cost can be about twice that of an adiabatic LES (Kraus et al. 2018). However, due to the uncertainty and computational expenses involved, the influence of non-adiabatic conditions in conjunction with non-adiabatic flamelets (Massey et al. 2021) on the thermoacoustic aspects is beyond the scope of this study. This will be explored in the future.

All simulations are performed using OpenFOAM v7 with a compressible PIMPLE algorithm (rhoPimpleFoam solver). Second-order central difference schemes are used for the spatial derivatives and a first-order implicit Euler scheme is used for the temporal derivatives. A small time step of $\Delta t = 0.25 \mu\text{s}$ is used to ensure numerical stability. The resulting CFL number remains below 0.4 for the entire domain. After reaching a stationary state, time-averaged statistics are collected for about 0.2 s which corresponds to 12–15 characteristic flow-through-times based on the entire domain length and bulk mean velocity of air at the inlet. The simulations are run on ARCHER2, a UK high-performance computing facility, using 1536 cores and each case requires 90 h of wall clock time.

4 Results

4.1 Non Reacting Flow Field

The non-reacting case NR listed in Table 1 is used to assess the grid dependency using two grids with 2 million (2M) and 8 million (8M) cells. The grid resolution is increased (from $\delta x \approx 2$ to 0.8 mm) only in the fine cell regions (covering parts of the air plenum, fuel plenum swirler and combustion chamber) visible in Fig. 1b and the cell sizes in the remaining regions are approximately same in both grids. Measured time-averaged and root-mean-square (rms) values are compared with the LES results in Fig. 2 at four stream-wise, z , locations where the origin is at the tip of the centrebody cone as shown in Fig. 1a. The computed rms values are obtained using only the resolved variance ($\langle \tilde{U}^2 \rangle - \langle \tilde{U} \rangle^2$) to understand the effects of the grid independent of the sub-grid model.

The results show weak sensitivity to the grid, as both the 2M and 8M grids give reasonable agreement with the measurements. The 8M grid performs slightly better than the 2M grid by capturing the peaks of the axial velocity profiles depicted in Fig. 2a and b. Although the size of the Inner Recirculation Zone (IRZ) is better captured with the 8M grid (see Fig. 2a), the differences are less than 10%. The differences in the x -direction velocities for the two grids are mostly within 10%, but some discrepancies close to the wall in the most downstream location is observed which is because of the lower resolution close to the wall at this streamwise location.. The velocity gradients for the y -direction velocity are better captured by the 8M grid. However, a discrepancy in the $\sqrt{\langle \sigma_w^2 \rangle}$ values near the IRZ is noticeable in Fig. 2f, but it is important to consider the larger uncertainties in the Particle Image Velocimetry (PIV) measurements for the out-of-plane velocity W in this context. Overall, the 8M grid shows comparable results with the 2M grid and captures the flow field satisfactorily. The performance of the two grids is also assessed using Pope's criterion (Pope 2000; Chen and Swaminathan 2020) which is given by

$$\frac{k_{\text{res}}}{k_{\text{tot}}} = \frac{k_{\text{res}}}{k_{\text{res}} + k_{\text{sgs}}} \geq 0.8, \quad (6)$$

where k_{res} is the resolved kinetic energy given by

$$k_{\text{res}} = \frac{1}{2} (\langle \sigma_u^2 \rangle + \langle \sigma_v^2 \rangle + \langle \sigma_w^2 \rangle) \quad (7)$$

and the sub-grid kinetic energy k_{sgs} is approximated as Pope (2000) $k_{\text{sgs}} \approx \frac{3}{2} u_\Delta'^2$. The sub-grid scale velocity is modelled using the scale similarity model (Pope 2000; Chen and Swaminathan 2020), $u_\Delta' = |\tilde{\mathbf{U}} - \hat{\mathbf{U}}|$, where $\tilde{\mathbf{U}}$ is the filtered velocity vector and $\hat{\cdot}$ denotes a test-filtering operation. Figure 3 shows that the Pope's criterion is sufficiently satisfied by both 2M and 8M grids with the 8M grid performing better because of the higher resolution. Since finer cells will be required to resolve the increase in rms values in the reacting flow, the 8M grid is used for reacting conditions.

4.2 Reacting Flow Field

Figure 4 displays the computed and measured streamlines along with the contours of time-averaged axial velocity in the combustor for case H0, illustrating the characteristic

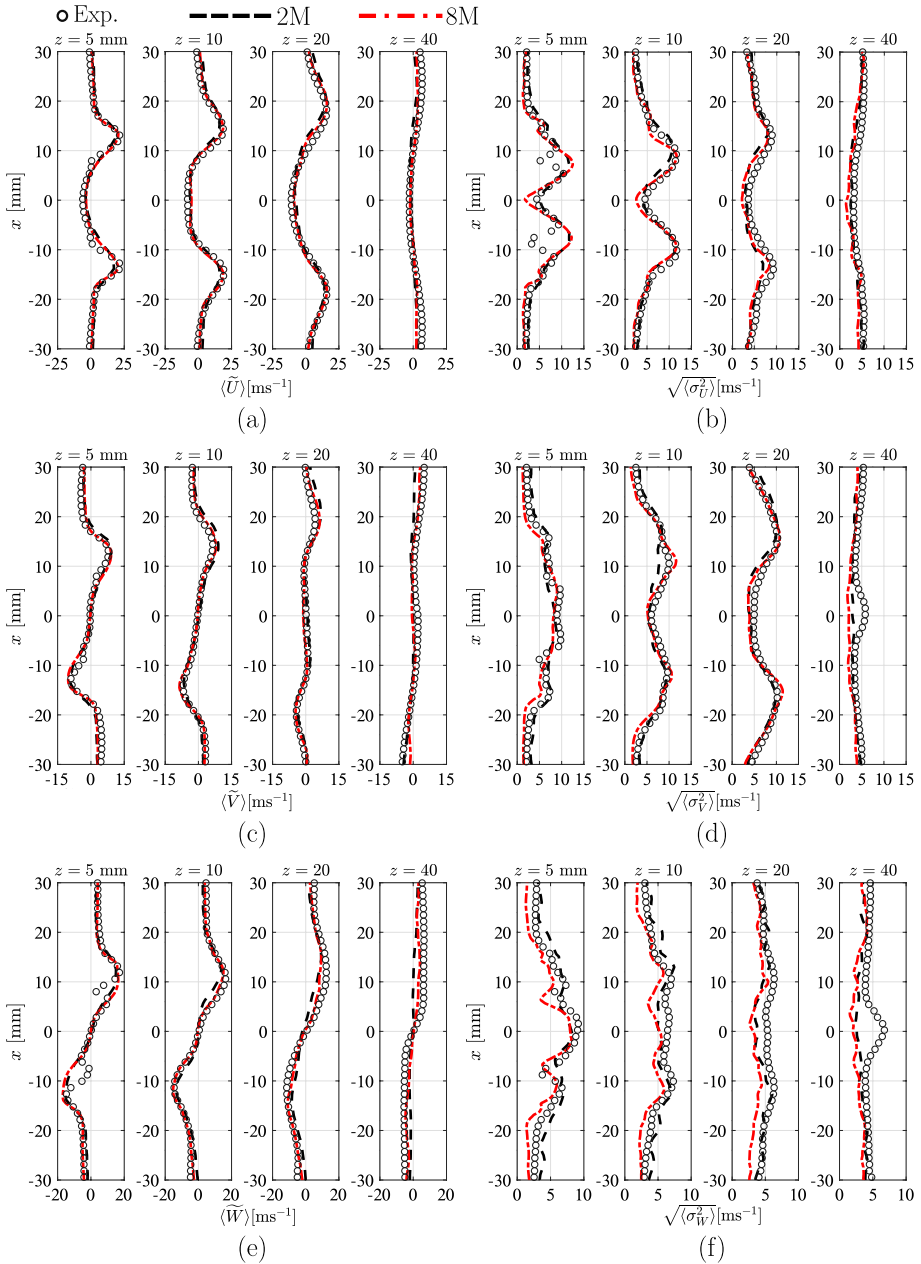


Fig. 2 Cold flow comparison of axial, x-direction and y-direction velocity variations for four streamwise locations. Symbols: measurements, lines: LES using 2 different grid resolutions

features of a swirling flow jet. The streamlines show the Outer Recirculation Zone (ORZ) near the combustor corners, two axial jets, and the IRZ composed of two asymmetric Vortex Breakdown Bubbles (VBB). The upstream VBB exhibits an asymmetry as seen by the

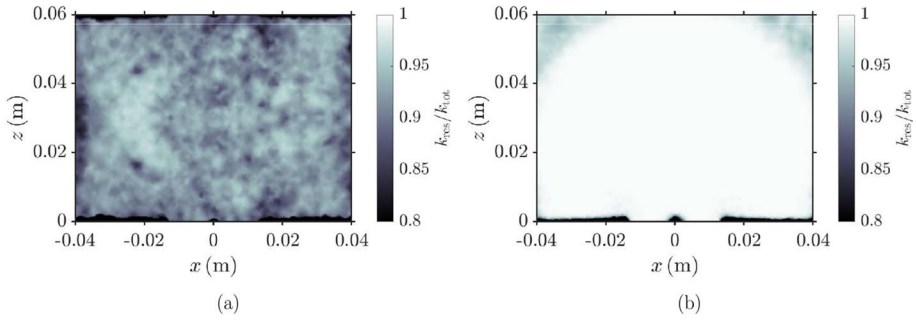


Fig. 3 Ratio k_{res}/k_{tot} for **a** 2M and **b** 8M grids

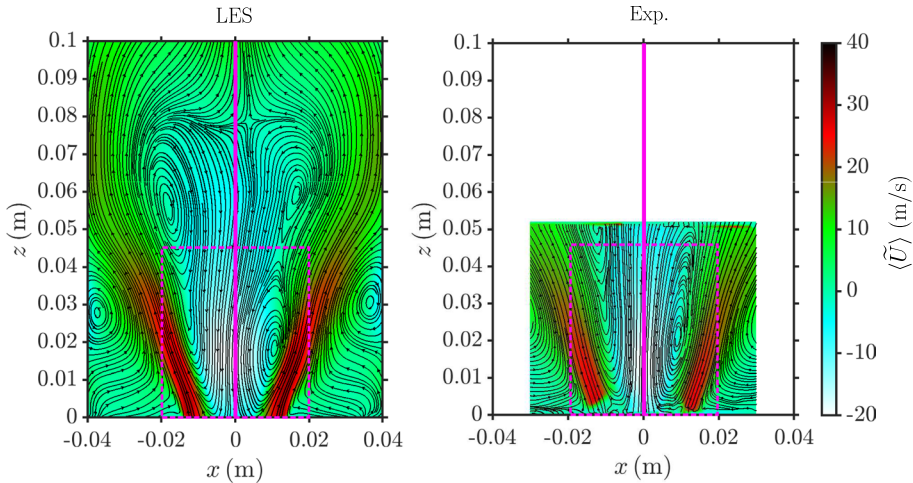


Fig. 4 Comparisons of computed and measured streamlines of time-averaged axial velocity for case H0. The colour indicates the axial velocity

differences in the flow field between the left and right halves as highlighted using a rectangular box in Fig. 4 (see also Fig. 5). The left-hand side of the pink box in both Fig. 4a and b indicate recirculation without a distinct bubble. The downstream VBB is only partially visible in the measurements due to being further downstream of the PIV measurement window. Despite slight differences both measurements and computations indicate an asymmetry that cannot be attributed to incoherent turbulent fluctuations. This suggests that the asymmetry is due to the presence of an intermittent coherent oscillation. Since the bulk flow is a swirling jet, this suggests the presence of an intermittent PVC which is consistent with the recent study (Datta et al. 2022). Note that the averaging window for PIV spans 1 s whereas it is 0.2 s in LES for both H0 and H20. While the averaging window is shorter for LES, it is still approximately 100 times the $1/f_{PVC}$ ($f_{PVC} \approx 500$ Hz). Statistics collected at later times (0.3 s and 0.4 s—not shown) reveal no significant difference in the flow field and we conclude that the LES flow field is statistically stationary.

The length of the VBB is about 0.045 m in Fig. 4a and about 0.05 m in Fig. 4b. The computations show a wider upstream bubble compared to experiments (maximum width of 0.015 m in LES compared to 0.012 m in experiments) for case H0, due to the wider

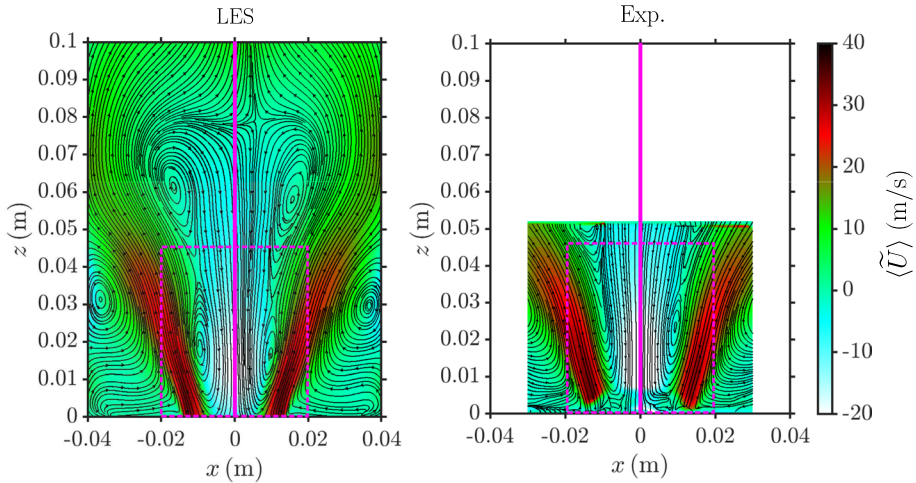


Fig. 5 Comparisons of computed and measured streamlines of axial time-averaged velocity for case H20. The colour indicates the axial velocity

jet angle resulting from the intense flame flapping due to large amplitude thermoacoustic oscillation (see Fig. 26). Swirl number fluctuations (studied in Sect. 4.4) induced by the thermoacoustic oscillation result in this flame flapping motion and has been studied previously (Candel et al. 2014). It will be shown in Sect. 4.3 that the amplitude of thermoacoustic oscillation is overestimated for this case, which is the likely cause of these discrepancies in the flow field. Additionally, the further upstream flame stabilisation in LES due to adiabatic boundary condition augments the flame flapping further which can result in these discrepancies. Past studies on this geometry (Fredrich et al. 2021a; Agostinelli et al. 2022) and other geometries (Chen et al. 2019b; Chen and Swaminathan 2020) have similar discrepancies due to overestimated thermoacoustic amplitude. This aspect is also clearly visible from the visualisation of the flow field depicted in Figs. 26 and 27 in the “Appendix 1”. Figure 5a shows a slight asymmetry and the maximum length of the upstream VBB is about 0.035 m compared to about 0.032 m in Fig. 5b. The maximum width of the VBB is about 0.01 m in Fig. 5a whereas the maximum width in Fig. 5b is about 0.006 m. The left-hand side of the pink box in Fig. 5a features a distinct VBB whereas the bubble in Fig. 4b is more subtle and narrow. These differences arise due to the overestimated thermoacoustic oscillation which significantly moderates the flow field as indicated previously and in past work (Shanbhogue et al. 2016; Meier et al. 2007). The computed jet, ORZ, and IRZ features of the bulk flow are similar to the measurements, with important details such as the twin asymmetric VBB being reproduced.

In Fig. 5, the computed and measured streamlines are presented along with the contours of time-averaged axial velocity in the combustor for case H20. The higher reactivity of hydrogen is evident from the slightly higher axial jet velocities, which result from the higher volumetric expansion. The streamlines show bulk flow features similar to those of the pure methane case, with notable differences in the upstream VBB. With the addition of hydrogen, the upstream VBB becomes nearly axisymmetric which is consistent with the measurements. The length of the upstream VBB/IRZ is smaller in the presence of hydrogen, which is likely due to decreased radial pressure forces resulting from a higher local heat release rate consistent with Massey et al. (2019). Other reasons include the higher

amplitude of thermoacoustic oscillations in H₂O (shown in Sect. 4.3) and flame flashback which modulate the flow reversal in IRZ (see Fig. 27) and ultimately affect both radial and axial pressure forces within the IRZ. The reasons for reduction in IRZ length with increase in local heat release require further analysis which is not the focus here. The loss of asymmetry is due to the suppression of intermittent helical instabilities near the dump plane, as reported in Datta et al. (2022). The loss of asymmetry and its link with helical instabilities is addressed further in the subsequent sections.

Figure 6 illustrates the comparisons of time-averaged statistics between the computed and measured mean and rms velocities for case H₀. The LES results follow the trends of the measurements, with a maximum overestimation in peak axial velocities of about 10%. The velocity gradients in the shear layer ($5 < |x| < 15$ mm) capture the trend of the measurements. The LES captures the backflow axial velocity well as seen in Fig. 6a. However, the width of the IRZ is slightly overestimated as mentioned in the discussion of Fig. 4, which is related to the overestimation in thermoacoustic amplitude (Agostinelli et al. 2022; Fredrich et al. 2021a) to be discussed in Sect. 4.3. The discrepancy in the y -direction velocity is the result of intense flame flapping due to high-amplitude thermoacoustic oscillation. The overestimation in rms velocities in some locations (for example, see $z = 10$ mm for both cases) is also related to the intense flame flapping. Past studies in this geometry (Fredrich et al. 2021a; Agostinelli et al. 2022) and other swirling flame configurations (Chen et al. 2019a; Chen and Swaminathan 2020) have shown that these discrepancies can arise from the overestimation of the thermoacoustic amplitude. The intense modulation of the flow field during one cycle of the thermoacoustic oscillation is clearly visible in Figs. 26 and 27 which suggests that the overestimation in thermoacoustic amplitudes can be the reason for such discrepancies. Also, note that PIV usually has an uncertainty varying from about 1 m/s for in-plane velocities to 3 m/s in out-of-plane velocities (Kumar et al. 2023). However, the specific uncertainties for these cases are not available. Such discrepancies are a common feature of LES results of the PRECCINSTA burner as shown in Fredrich et al. (2021a), Agostinelli et al. (2022). The PIV measurements are significantly affected by distortions close to the dump plane, which explains the overestimation in rms values close to those locations.

Similarly, Fig. 7 show the comparisons of time-averaged statistics between the computed and measured mean and rms velocities for case H₂O. The LES results follow the trends of the measurements especially in capturing the reverse flow and peak axial velocities to within 10%. The locations of peak jet velocity and the maximum width of the IRZ are within 20% of the measurements. The trends of increasing peak x -direction and y -direction velocities with hydrogen enrichment are captured by the LES, with a maximum discrepancy in peak velocities of about 10%. The discrepancy in the y -direction velocity is likely to be associated with the slightly higher amplitude of thermoacoustic oscillation, which will be shown in the subsequent sections. The computed rms velocity are mostly within 20% of the measurements. Note that the computed rms values shown in Figs. 6 and 7 correspond to only the resolved field, suggesting that the large scale turbulence upto 20% of the experimental rms velocity field is resolved by the computational grid. The flame flapping motion results in a slight overestimation of axial rms fields as discussed previously. The distortion of the PIV measurements due to reflection from the dump-plane is the reason for the significant overestimation of rms velocities at $z = 5$ mm. A similar distortion of the experimental results due to reflection from the side walls is also visible in Fig. 7f at $z = 10$ mm. Figure 8 shows the histogram of normalised filter width sizes ($\Delta^+ = \delta x / (\delta_L^+)_st$) where δx is the cell size given by the cube root of the cell volume and $(\delta_L^+)_st$ is the laminar flame thickness at the stoichiometric equivalence

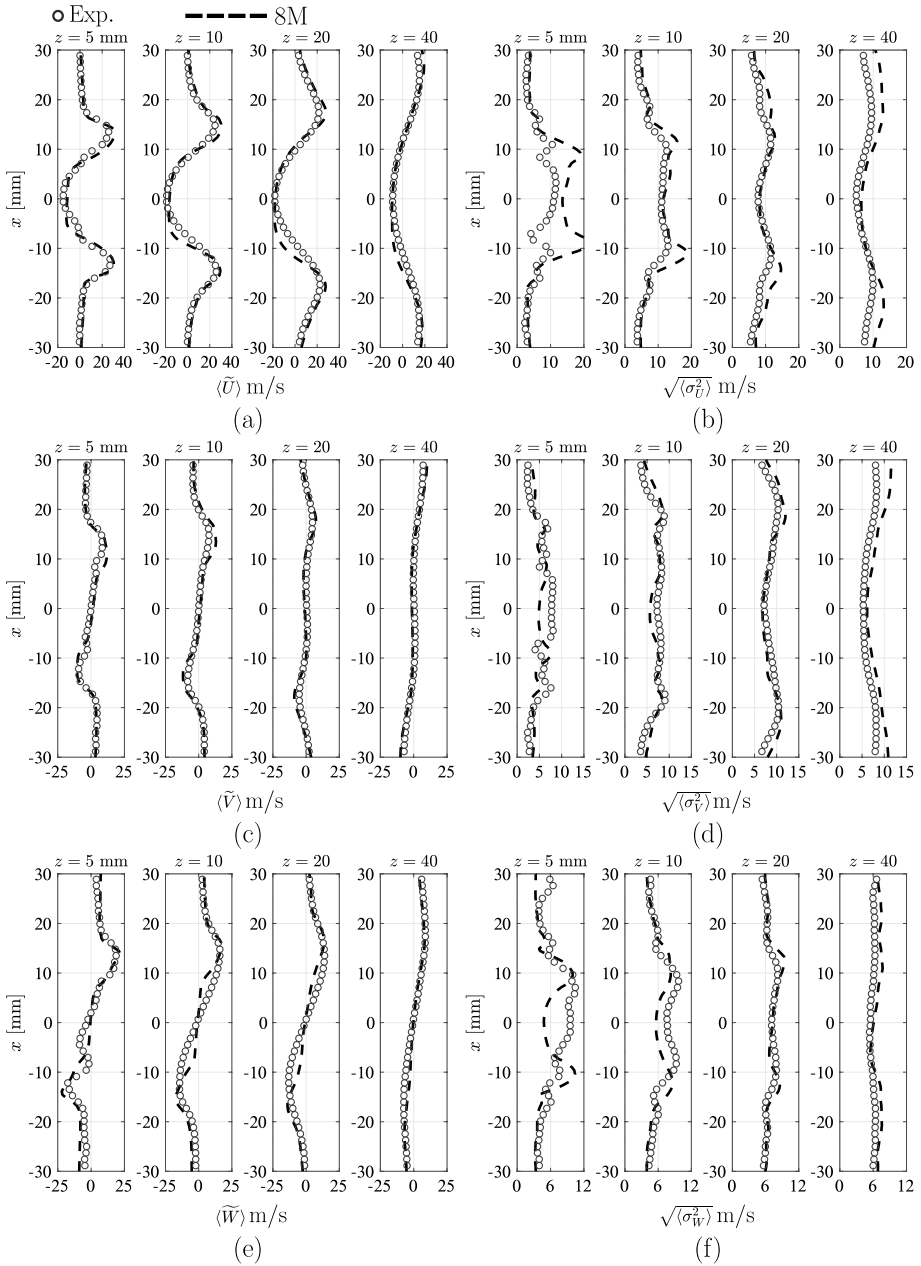


Fig. 6 Typical comparisons of measured (symbols) and computed (lines) of time-averaged mean (a, c, e) and rms (b, d, f) velocities for case H0. a, b Axial velocity, c, d x-direction velocity and e, f y-direction velocity

ratio. The distribution clearly shows that most cells sizes are close to the laminar flame thickness suggesting that the combustion occurs at sub-grid scales which are modelled using the methodology described in Sect. 2. Past studies (Chen et al. 2019a; Massey

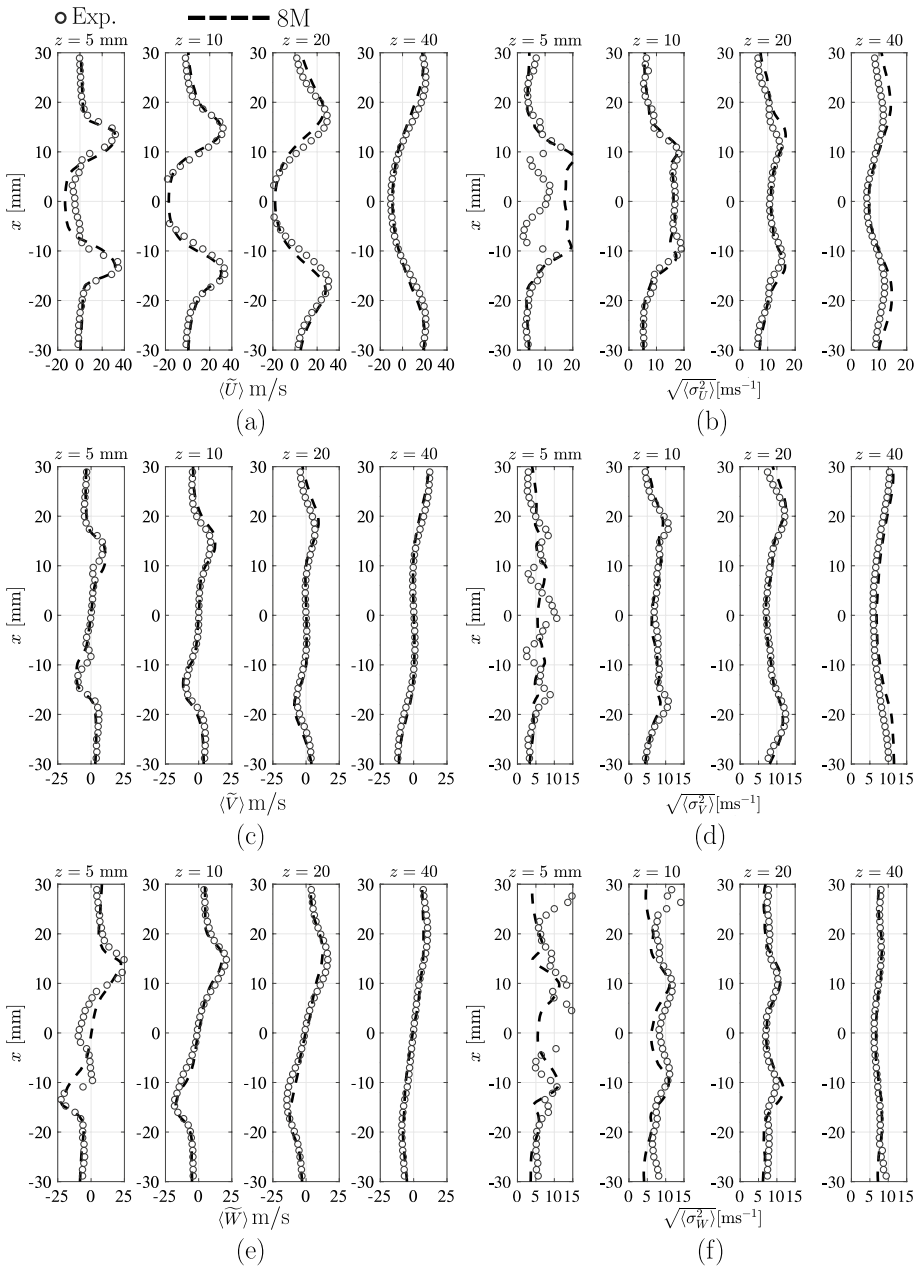


Fig. 7 Typical comparisons of measured (symbols) and computed (lines) of time-averaged mean (a, c, e) and rms (b, d, f) velocities for case H2O. a, b Axial velocity, c, d x-direction velocity and e, f y-direction velocity

et al. 2019) have shown that a grid cell distribution with cell size within $\Delta^+ \approx 2$ is satisfactory for reactive flows. A grid dependency study for the reacting flows is not required

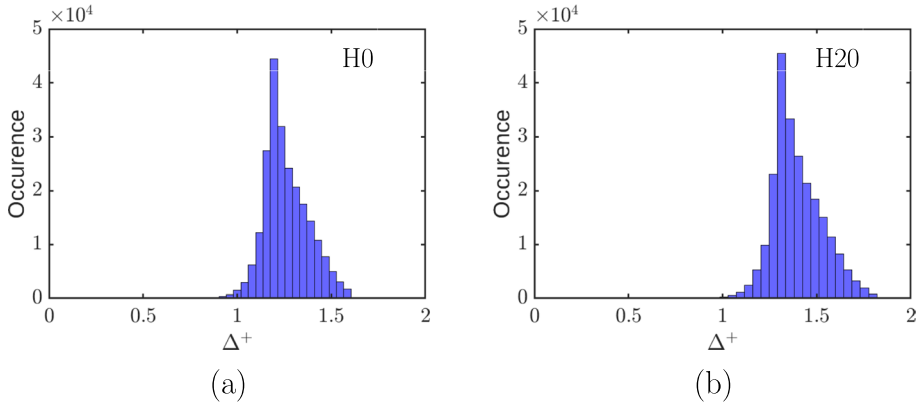


Fig. 8 Histograms of the normalised filter width $\Delta^+ = \delta x / (\delta_L^2)_{st}$ distribution for **a** H0 and **b** H20, where the cell samples are collected within the reaction region marked using $\langle \bar{\omega}_c \rangle > 0$

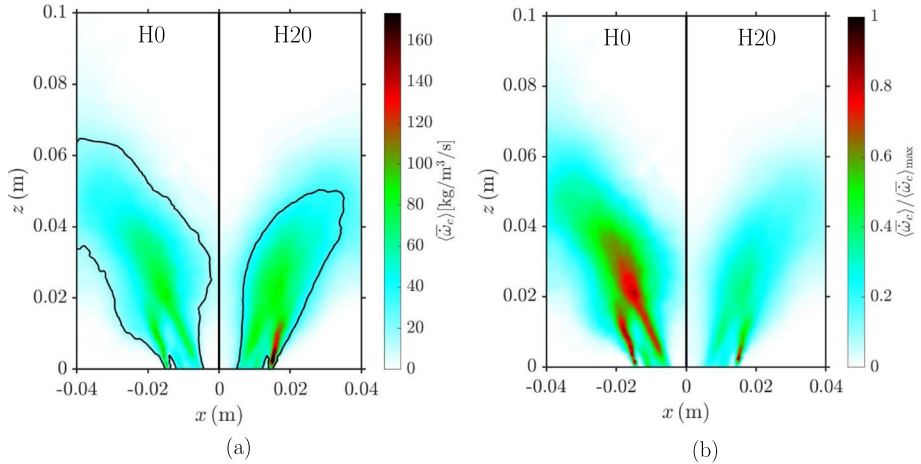


Fig. 9 Mid-plane contours of **a** time-averaged reaction rate, $\langle \bar{\omega}_c \rangle$ and **b** normalized time-averaged reaction rate $\langle \bar{\omega}_c \rangle / \langle \bar{\omega}_c \rangle_{max}$ for case H0 and H20. Black line indicates a contour line with a value of 15% of maximum reaction rate

since the model used for SGS combustion has the ability to adopt to the local changes in flow and chemical processes and their interactions in a statistical sense.

Figure 9a shows the time-averaged reaction rate contours, $\langle \bar{\omega}_c \rangle$ for cases H0 and H20. The V-flame characteristic of swirl-stabilized flames is evident in both cases. Note that the two flame branches on the inner and outer shear layer are part of the same branch of the “V” structure. The addition of hydrogen slightly increase the local heat release rates near the dump-plane and reduces the flame length as seen from the black contour line corresponding to the 15% of maximum reaction rate in Fig. 9a. It will be shown in Sect. 4.4 that the resulting upstream traversal of the VBB along with additional effects related to Swirl number fluctuations suppresses helical motions yielding a symmetric

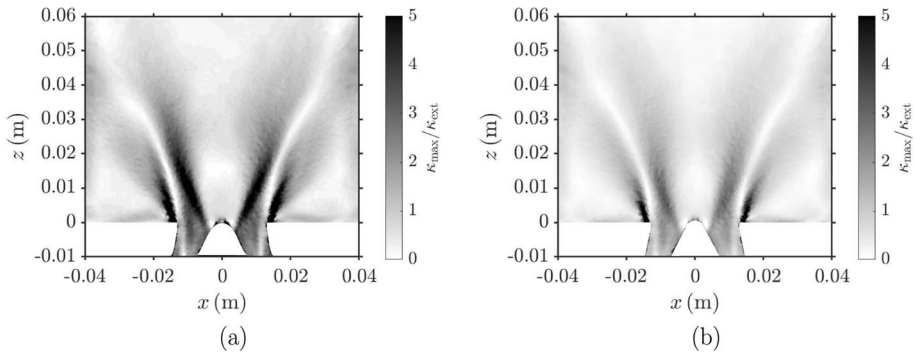


Fig. 10 Normalised maximum in-plane principal extensional strain rate ($\kappa_{max}/\kappa_{ext}$) for **a** H0 ($\kappa_{ext} = 799 \text{ s}^{-1}$) and **b** H20 ($\kappa_{ext} = 1410 \text{ s}^{-1}$)

upstream VBB. The upstream traversal of the VBB resulting in suppression of the PVC is consistent with the recent study by Datta et al. (2022). The higher reaction rates and the resulting higher heat release qualitatively explains the decrease in the length of the upstream VBB (Massey et al. 2019) as discussed previously. The normalised time-averaged reaction rates are shown in Fig. 9b which reveals that case H20 has a slightly lower flame brush width than case H0 with a more uniform distribution of heat release rate.

The addition of hydrogen results in an increase in extinction strain rates as shown in Shanbhogue et al. (2016), Datta et al. (2022). Since the flow strain rates are nearly identical for the two cases, it was shown in Datta et al. (2022) that the higher extinction strain rates in case H20 is responsible for an attached flame. In this work, this aspect is confirmed by showing the ratio of the maximum in-plane principal extensional strain rate to the respective extinction strain rate (κ_{ext}) obtained from Datta et al. (2022) in Fig. 10. The extinction strain rate are obtained using the counterflow reactant-to-reactant configuration. Further details can be obtained in Datta et al. (2022). The maximum extensional strain rate κ_{max} is the maximum eigenvalue of the rate of strain tensor S given by

$$S = \frac{1}{2}(\nabla\tilde{U} + \nabla\tilde{U}^T). \tag{8}$$

It can be seen in Fig. 10a that κ_{max} is several times greater than the κ_{ext} in case H0. Contrastingly, Fig. 10b shows that in case H20 $\kappa_{max}/\kappa_{ext}$ is lower suggesting that case H20 is less prone to extinction by flow induced straining. The values in the nozzle are also lower for case H20 compared to H0, hence this is one of the many reasons that the flame in case H20 flashes back further upstream than case H0 as seen in Fig. 27. Other reasons for flame flashback include higher thermoacoustic amplitude, better mixing in the nozzle, etc. which are further analysed in the next section.

Figure 11a shows the radially-averaged distribution of time-averaged reaction rates, $\langle\bar{\omega}_c\rangle^\dagger = \frac{1}{w} \int_{-w/2}^{w/2} \langle\bar{\omega}_c\rangle dx$ for both cases, where w is the width of combustor. The addition of hydrogen appears to increase the reaction rates in the flame root. The extent of flame flashback is slightly higher in the presence of hydrogen due to its higher flame speed. The peak reaction rate in case H20 occurs approximately 6 mm upstream than in case H0. However, the flame tip distribution remains unchanged between the two cases. The radially averaged rms of the filtered reaction rate which is important to understand the thermoacoustic aspects

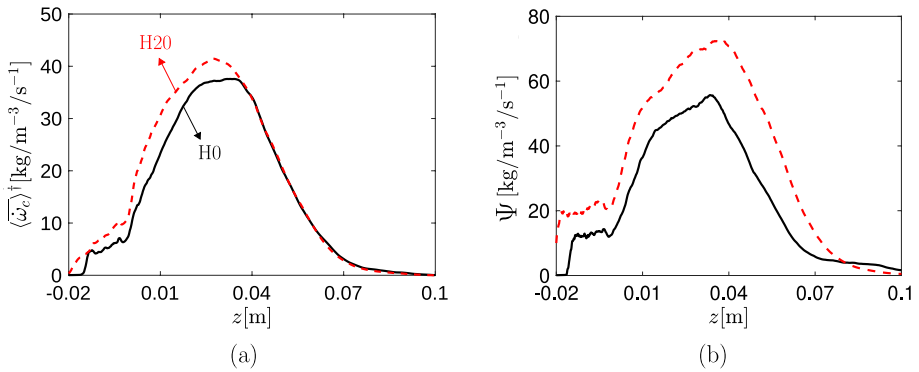


Fig. 11 Axial variation of radially-averaged **a** mean reaction rate, $\langle \dot{\omega}_c \rangle^\dagger$ and **b** rms reaction rate, Ψ , of the progress variable. The results are shown for cases H0 and H20

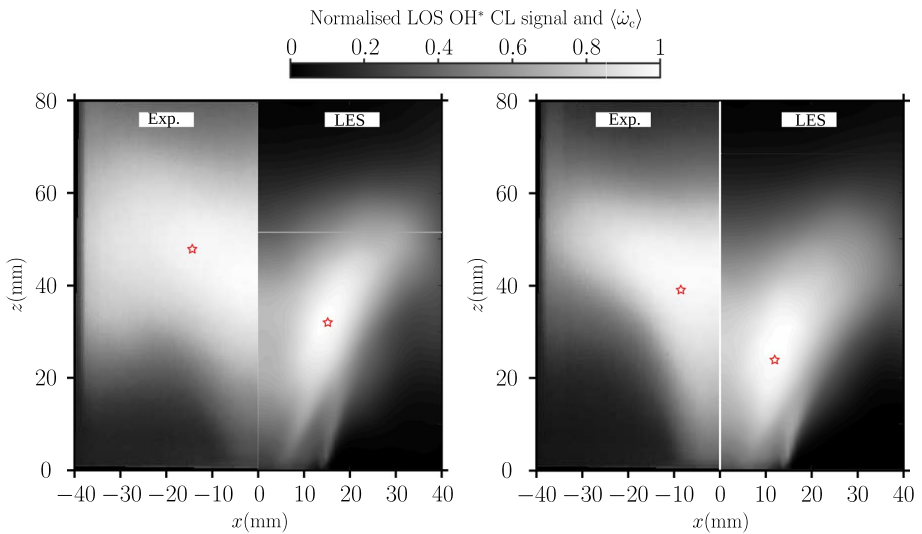


Fig. 12 Comparisons of LOS integrated OH* CL images and LOS integrated $\langle \dot{\omega}_c \rangle$ from LES for case **a** H0 and **b** H20. Red pentagram demarcates the maximum values

in Sect. 4.3 is also shown in Fig. 8b for both cases. This quantity is defined as $\Psi = \frac{1}{w} \int_{-w/2}^{w/2} \langle \{\overline{\dot{\omega}_c} - \langle \overline{\dot{\omega}_c} \rangle\}^2 \rangle^{\frac{1}{2}} dx$ and Fig. 11b clearly shows that the rms values in H20 case are larger than in H0. Specifically, the flame root which is located upstream of the dump plane fluctuates more in the H20 as indicated by the rms value for $z < 0$.

Figure 12 shows the Line-of-Sight (LOS) time-averaged mean reaction rates and the measured OH* Chemiluminescence (CL) fields which are used for qualitative comparisons. The LES manages to capture the trend of decreasing flame length characterised by the maximum value, although some notable differences can be observed. The differences close to the dump-plane in both cases is attributed to the adiabatic boundary condition

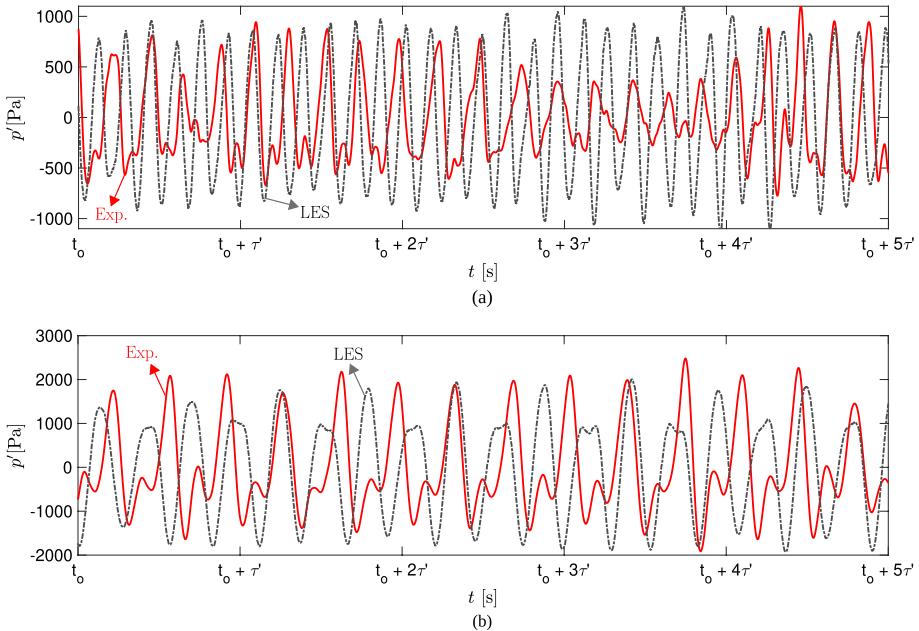


Fig. 13 Time series of pressure fluctuations at probe PP2 for case **a** H0 with $\tau' = 0.02s$ and **b** H2O with $\tau' = 0.007s$

used in the simulations. The adiabatic boundary condition on the dump-plane results in an outer flame close to the ORZ (see Fig. 9) as observed in Fredrich et al. (2019), Bénard et al. (2019). It should be noted that the lack of temperature measurements in the experiments makes the use of non-adiabatic boundary conditions challenging as discussed in Sect. 3. Therefore, the effect of non-adiabatic boundary conditions on the flame shape is not considered here. The resulting flame flashback results in larger consumption of reactants upstream of the dump plane which results in shorter flame in the LES compared to the experiments. The flame shape and size are within reasonable limits to capture important dynamics like transition to period-2 thermoacoustics and intermittent PVC dynamics which is the primary motivation behind this work. These aspects are discussed in the following sections.

4.3 Thermoacoustic Aspects

The pressure time-series $p(t)$ is measured and computed at probe PP2 in the combustor (see Fig. 1a). The pressure fluctuations shown in Fig. 13 obtained by subtracting the time-averaged pressure $\langle p \rangle$ from $p(t)$, which is denoted as $p'(t)$. Note that τ' is an arbitrary time window whose values are given in the caption of Fig. 13. The computed pressure oscillation has a maximum amplitude of approximately 1000 Pa and 2000 Pa for cases H0 and H2O respectively. It is observed that the time variation of measured pressure amplitude in case H0 is larger than the computed result as shown in Fig. 13a. The measured amplitude drops to approximately 250 Pa within the interval $t_0 + 3\tau' < t < t_0 + 4\tau'$ due to the intermittency in the pressure signal, which has been reported in Datta et al. (2022). This behaviour is

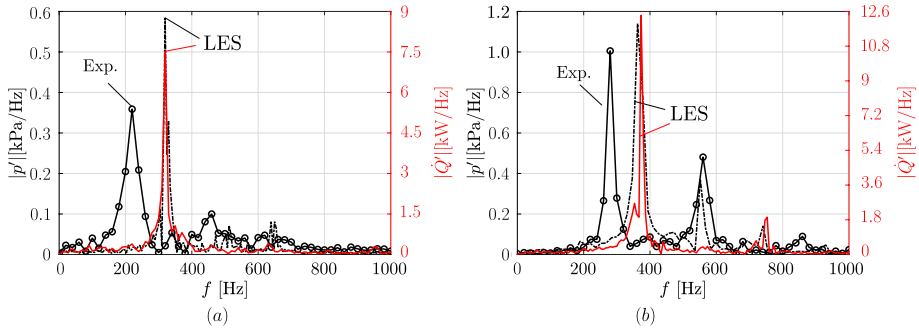


Fig. 14 Frequency spectrum of the measured and computed pressure and volume-integrated heat release rate fluctuations. The red solid line corresponds to the volume-integrated heat release rate fluctuations and black lines correspond to the measured (circled) and computed (dashed-dotted) pressure fluctuations at probe PP2 (see Fig. 1a)

associated with the intermittent flame lift-off from the centre cone resulting in a temporary loss of acoustic-heat release rate coupling and a subsequent reduction in pressure amplitude. Heat loss along the centre cone and dump-plane along with strong influx of velocity leads to flame lift-off and a lower extent of flashback in the experiments. While the velocity fields are satisfactorily reproduced, the lack of heat loss at the walls does not allow for the flame lift-off in the computations. Although the simulations indicate that the flame tends to lift-off (shown in Sect. 4.3), complete lift-off is prevented by the adiabatic boundary condition used on the center cone.

The frequency spectrum of measured and computed pressure and heat release rate for both cases are shown in Fig. 14. The peak is at approximately 300 Hz ($f_1 = 224$ Hz in the experiment) for case H0 with an overpredicted amplitude. This overestimated amplitude is due to the absence of (i) complete lift-off events in the LES and (ii) the damping caused by loosely fitted quartz walls in the experiments. The former aspect leads to low and high peak-to-peak pressure fluctuation amplitudes (Datta et al. 2022), as seen in the experimental pressure trace shown in Fig. 13 which leads to lower peak in the spectrum (averaging of low and high amplitudes). The latter aspect is a common feature of LES of thermoacoustically unstable cases as reported in Lourier et al. (2017), Agostinelli et al. (2022). As a result of the intermittent lift-off events, a delayed feedback response of the flame to acoustic and mixture fraction perturbations results in a lower frequency compared to the value computed in LES. This particular aspect will be discussed in more detail in this section.

The addition of hydrogen to the fuel mixture yields period-2 dynamics that are evident from two distinct peaks in the pressure spectrum displayed in Fig. 14b, as well as the alternate low and high-amplitude peaks depicted in Fig. 13b. The first and second peak depicted in Fig. 14 correspond to the plenum and chamber acoustic modes. The LES overestimates the amplitude of the first mode at $f_1 = 370$ Hz (283 Hz in the experiment) because of the second reason noted above. The overestimate of f_1 by about 76–87 Hz in the LES of H0 and H20 is because of large extent of flame flashback leading to quicker feedback. The computed second pressure mode at $f_2 = 548$ Hz is close to the experimental value of 568 Hz, and the amplitudes are within 20% of the measurements. The third peak observed at about 750 Hz is the harmonic of f_1 .

Figure 14 also shows the frequency spectrum of the volume-integrated heat release rate fluctuations for both cases. This fluctuation is $\dot{Q}'(t) = \dot{Q}(t) - \langle \dot{Q} \rangle$, where $\langle \dot{Q} \rangle$ represents

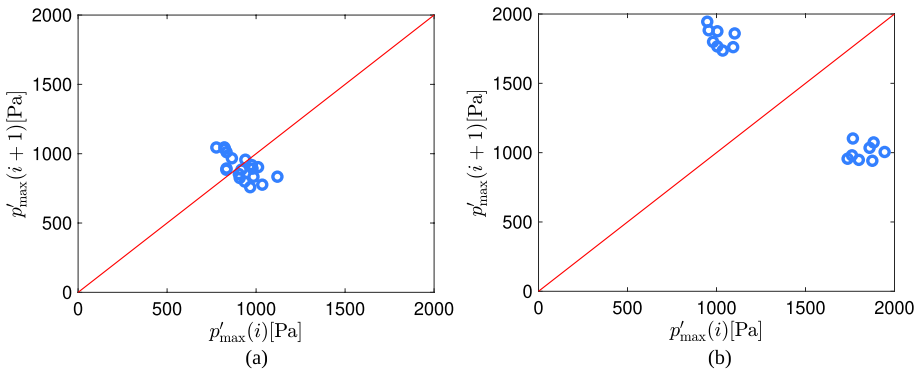


Fig. 15 Poincaré map of computed pressure at probe PP2 (see Fig. 1a) for case **a** H0 and **b** H20

time-averaged \dot{Q} , and $\dot{Q}(t) = \int_V \dot{q}(\mathbf{x}, t) dV$ with $\dot{q}(\mathbf{x}, t)$ denoting the local heat release rate per unit volume at the location \mathbf{x} and time t . This spectrum displays strong peaks at the first mode for both cases, while no peak is observed in the second mode. This indicates that the pressure and heat release rate fluctuations exhibit a 2:1 frequency-locking behaviour, consistent with the experimental results reported in Kushwaha et al. (2021) for case H20.¹ A similar 2:1 frequency-locking behaviour is observed in a recent study (Kumar et al. 2023), and the reasons have been attributed to interactions between the first and second mode through the first mode of heat release rate fluctuations. The differences between the LES and experimental results are attributed to heat loss at the walls and a detailed investigation on this point needs wall temperature data which is not available currently.

The Poincaré maps displaying the successive maxima in the time series of pressure fluctuations (see Fig. 13) for each case are presented in Fig. 15. For case H0, the map illustrates a single cluster, indicating a single period for the pressure oscillation. Due to the large temporal variations in amplitude, the cluster is relatively spread out on the map. The map reveals two distinct effects of hydrogen addition on the system's dynamics: an increase in the amplitude of fluctuations and the emergence of two distinct periods of oscillation as evidenced by the two clusters. Despite the fact that Fig. 11 illustrates only a minor impact on the time-averaged axial distribution of heat release rate, the system dynamics, specifically the LCO characteristics has changed significantly from period-1 to period-2. Recent studies (Agostinelli et al. 2022; Kumar et al. 2023) recognised the first and second modes as associated with the plenum and chamber modes respectively.

Previous studies (Meier et al. 2007; Franzelli et al. 2012; Lourier et al. 2017; Stöhr et al. 2017; Fredrich et al. 2021a, b) have shown that equivalence ratio fluctuations drive the thermoacoustic feedback loop in the PRECCINSTA burner. Figures 16 and 17 display the temporal evolution of the mixture fraction with a contour line of reaction rate corresponding to $\bar{\omega}_c = 0.3 \times (\bar{\omega}_c)_{\max}$. At instant t_1 , rich mixture pockets are visible in the nozzle in Fig. 16. These pockets are then transported downstream into the combustion chamber from

¹ Note that the cases H0 and H20 reported in Kushwaha et al. (2021) are erroneously listed as CO1 (chaotic). These are actually period-1/P1 (can also be considered as weakly period-2/P2 due to low amplitude second peak seen in Fig. 14 and intermittent (Datta et al. 2022) as discussed) and period-2/P2 respectively. This aspect has been confirmed by personal communication with the authors and an erratum has been published (Kushwaha et al. 2023).

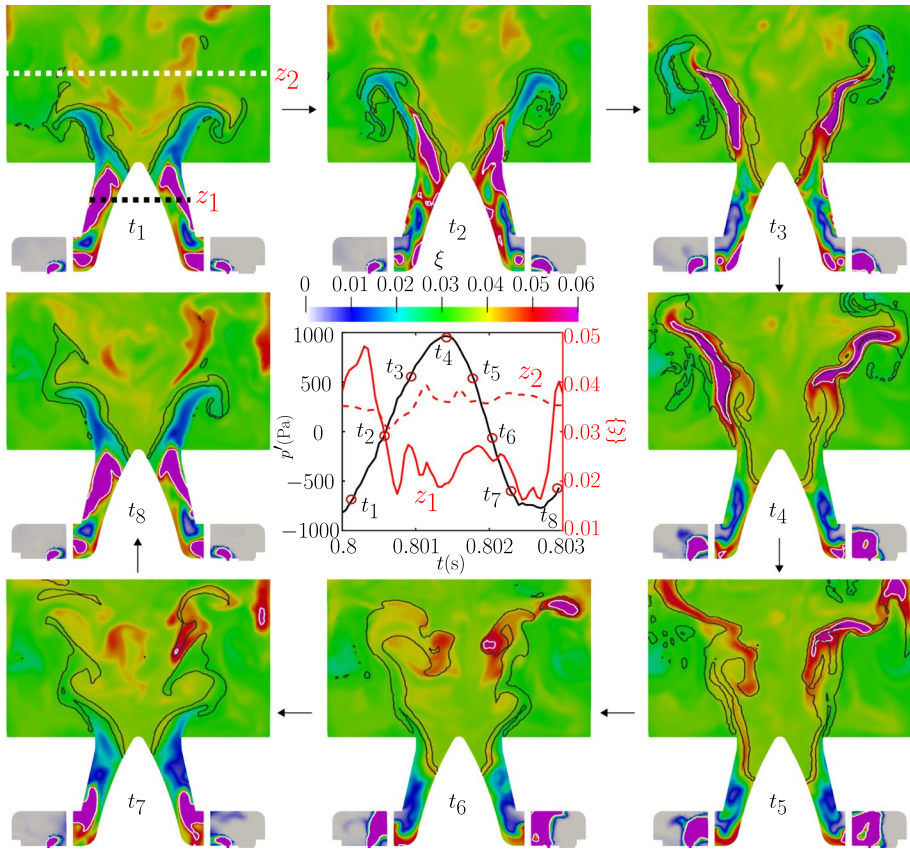


Fig. 16 Temporal evolution of the local reaction rate contour (black line corresponding to $\dot{\omega}_c = 0.3 \times (\dot{\omega}_c)_{\max}$) and mixture fraction for case H0 during one cycle of the fundamental mode. White contour lines correspond to stoichiometric mixture fraction $\xi_{st} = 0.055$. The centre frame shows the combustor pressure signal at probe PP2 and the area-averaged ($\langle \cdot \rangle$) mixture fraction at two planes $z_1 = -0.016$ m and $z_2 = 0.03$ m

time t_2 to t_5 , during which the flame cone angle narrows and its length increases dramatically due to flashback. The rich pockets in the combustor are then consumed, resulting in an increase in heat release (see Fig. 26 in Appendix 1). The acoustic wave travelling upstream modulates the air flow rate of the air stream more than the fuel flow rate (Franzelli et al. 2012; Fredrich et al. 2021a, b) due to the differences in acoustic impedance for the two streams. This results in a reduction of air flow rate compared to the fuel flow rate. Fuel then accumulates in the swirler during this period as observed in previous studies (Franzelli et al. 2012; Fredrich et al. 2021a, b). The axial velocity increases in the nozzle during instants t_6 to t_8 , carry the fuel-rich pockets downstream, which completes the cycle. At instant t_6 and t_7 , the flame can be seen to be stabilised on the centerbody cone even in the absence of a stagnation point suggesting that the adiabatic boundary is supporting the stabilisation rather than the flow. In the presence of heat loss, like in the experiments, lift-off events can be expected due to such high axial velocities and lack of stagnation points in nozzle. This is indeed the case as reported in Datta et al. (2022). The flame widens and gradually becomes shorter during this t_6 to t_8 period as observed in Fig. 16. Also, it is worth

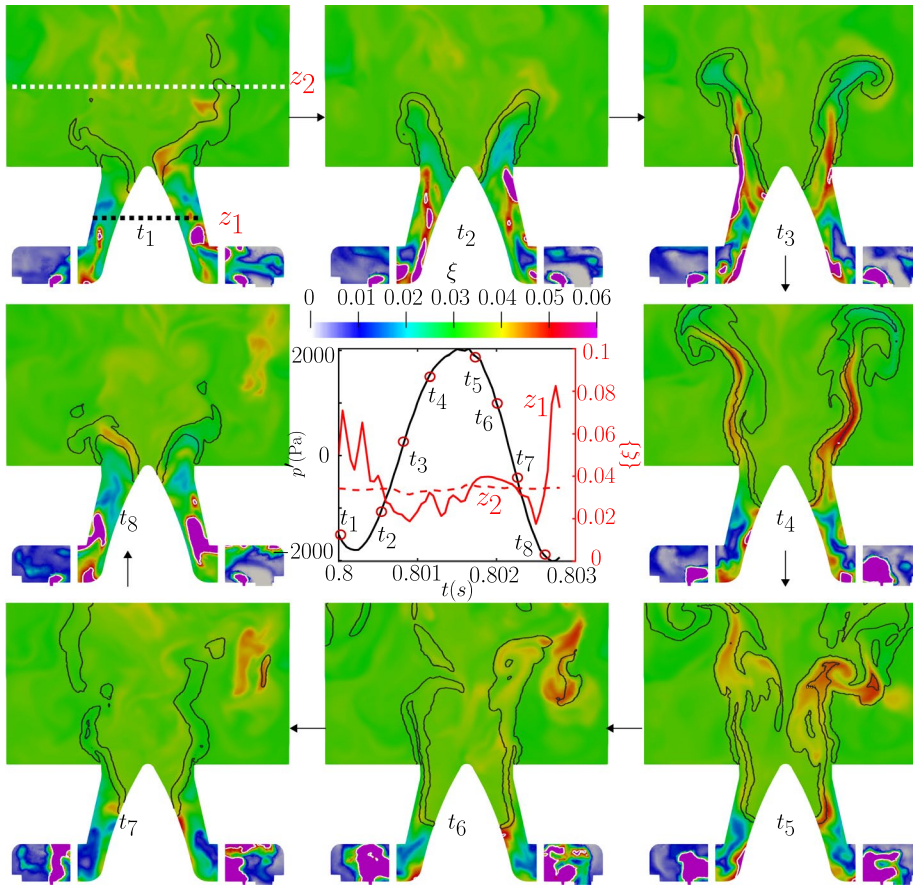


Fig. 17 Temporal evolution of the local reaction rate contour (black line corresponding to $\dot{\omega}_c = 0.3 \times (\dot{\omega}_c)_{\max}$) and mixture fraction for case H20 during one cycle of the fundamental mode. White contour lines correspond to stoichiometric mixture fraction $\xi_{st} = 0.053$. The centre frame shows the combustor pressure signal at probe PP2 and the area-averaged ($\langle \cdot \rangle$) mixture fraction at two planes $z_1 = -0.016$ m and $z_2 = 0.03$ m

noting that the significant flame flapping and flashback seen in this figure is overestimated, which results in discrepancies in velocity statistics as discussed earlier (see Fig. 6).

The inset of Fig. 16 shows the variation of area-averaged mixture fraction at two axial planes $z_1 = -0.016$ m and $z_2 = 0.03$ m. The entire fluid domain in each plane is considered for the averaging process. The fluctuations in the nozzle are far greater than in the combustor (rms of $\langle \xi \rangle$) is $\langle \{\xi\}^2 \rangle^{1/2} = 0.0086$ at z_1 and $\langle \{\xi\}^2 \rangle^{1/2} = 0.0019$ at z_2) because of the better mixing due to intense vortical motions visible in Fig. 26. The time-averaged mean ($\langle \xi \rangle$) of area-averaged mixture fraction at z_1 is 0.027 which is significantly below the global mixture fraction $\xi_{\text{glob}} = 0.038$.

In case H20, a similar cycle occurs, but there are three notable differences compared to H0. Firstly, during instants t_1 and t_8 , the flame length is much shorter compared to H0 due to the higher reactivity of hydrogen. Secondly, the flame flashback is significantly higher, along with a higher heat release close to the flame root, as shown in Figs. 11 and 27. Flame

flashback is governed by several factors such as flow-induced straining, extinction strain rates, local reaction rates/flame speed, local mixing, higher diffusivity, thermoacoustic amplitude and heat loss. The presence of hydrogen in the flammable mixture increases the extinction strain rates (Ren et al. 2001; Shanbhogue et al. 2016; Datta et al. 2022) ($\kappa_{\text{ext}} = 799 \text{ s}^{-1}$ in H0 and $\kappa_{\text{ext}} = 1410 \text{ s}^{-1}$ in H20). Since the operating conditions (thermal load, air/fuel flow rates and equivalence ratio) are nearly identical for H0 and H20, resulting in similar flow fields (time-averaged negative axial velocity along the centerline) for the two cases, flashback is because of stronger flame root (less prone to extinction). It is worth noting that the values of κ_{ext} reported in Shanbhogue et al. (2016) are for an adiabatic opposed axi-symmetric jet configuration, and therefore heat loss is not accounted for. However, heat loss will only act to reduce the extent of flame flashback. Additionally, higher diffusivity of hydrogen (included at the flamelet level in this study), better mixing and higher thermoacoustic amplitude also increase the likelihood of flame flashback.

Finally, the mixture fraction contours of H20 exhibit a more uniform distribution, as shown in Fig. 17. At z_1 , the time-averaged mean $\langle \xi \rangle$ of the area-averaged mixture fraction fluctuations is 0.036, which is higher than that of case H0 and closer to the global mixture fraction. While richer pockets are visible in H0 compared to H20, a large number of lean pockets are also visible, resulting in a lower time-average for H0. Additionally, the mixture fraction levels in the swirler section are higher in H20 due to the intense flapping of the fuel jet. The temporal variation of the area-averaged mixture fraction ($\langle \xi \rangle$) at z_2 is lower in H20 compared to H0 ($\langle \xi'^2 \rangle^{1/2} = 0.001$ at z_2 for H20). This is due to the higher levels of turbulence, as indicated by the higher rms velocities in Fig. 7 and better mixing in the swirler due to the intense flame flapping.

The better mixing in H20, resulting from higher turbulence levels, leads to a slightly leaner flame than in H0, as evidenced by the less common stoichiometric mixture fraction contours around the flame in Fig. 17. Despite the leaner mixture, the higher reactivity of hydrogen and better mixing result in higher local reaction rates (see Figs. 11a, 4 and 5 in “Appendix 1”), which contribute to the larger extent of flame flashback. The higher velocity fluctuations result in higher heat release rate fluctuations (see Fig. 11b). The higher local reaction rate fluctuations cause higher pressure fluctuations, which modulate the air and fuel stream more intensely. The resulting mixture fraction and velocity fluctuations then drive the heat release rate fluctuations, closing the feedback loop.

Due to the greater extent of flame flashback and higher consumption rates in H20, the flame responds more quickly to fluctuations in convected mixture fraction, resulting in a higher frequency of response. To further explain this point, the following phenomenological arguments are used. It is common practice to express the frequency of thermoacoustic oscillation as the Helmholtz resonator frequency, which can be calculated as $f_H \approx Kc/2\pi$, where K is a constant associated with the geometry, and c is the speed of sound. Since the speed of sound is primarily determined by the temperature field, which is nearly identical for the two cases (not shown), the increase in the thermoacoustic frequency upon adding hydrogen cannot be solely explained by the Helmholtz resonator frequency. The thermoacoustic frequency is also affected by time delays associated with fluid mechanical and combustion processes.

The feedback loop consists of three physical processes, each with its own time scale. These are: (i) convection of mixture fraction perturbations from the injection point to the flame (τ_{conv}), (ii) consumption of mixture inhomogeneities by the flame resulting in heat release rate fluctuations (τ_c), and (iii) generation of pressure perturbations that traverse upstream towards the injection point and modulate the fuel and air streams (τ_a). The time taken to complete one cycle of the thermoacoustic instability is expressed as

Table 2 Parameters governing the time scale of feedback loop

Case	l (m)	U_b (m/s)	u'/S_L	δ_F (m)	S_T (m/s)	τ (ms)	$1/f_1$ (ms) (LES)
H0	0.050	35	88	0.029	13	3.65	3.33
H20	0.045	35	91	0.022	18	2.50	2.70

$\tau \sim \tau_{\text{conv}} + \tau_c + \tau_a$. The convective time scale τ_{conv} can be expressed as $\tau \sim l/U_b$, where l is the convective length scale from the fuel nozzle to the point of maximum reaction rate as marked in Fig. 12, and U_b is the bulk mean velocity. The length scale is taken until the root of the flame since the mixture fraction fluctuations further downstream are close to one order of magnitude lower ($\langle \xi'^2 \rangle^{1/2} = 0.0129$ at z_1 and $\langle \xi'^2 \rangle^{1/2} = 0.001$ at z_2 for case H20). As the root of the flame is shifted slightly upstream in H20 (see Fig. 11a and b), $l_{\text{H0}} > l_{\text{H20}}$. The operating conditions ensure that the bulk mean velocities are nearly identical, and hence $\tau_{\text{conv,H0}} > \tau_{\text{conv,H20}}$.

The turbulent flame speed, S_T and consumption rate increases (Garcia et al. 2023) with hydrogen addition and hence $\tau_{c,\text{H0}} > \tau_{c,\text{H20}}$, where $\tau_c \sim \delta_F/S_T$ and δ_F is flame brush thickness. The flame brush thickness is approximated as the maximum width of the flame brush demarcated by the $0.15 \times \langle \bar{\omega}_c \rangle_{\text{max}}$ contour line as shown in Fig. 9a. Also, the consumption rate is higher in H20 because of the higher turbulence levels as seen in Fig. 7b, d and f. The correlation between turbulent flame speed and turbulence intensity in Kolla et al. (2010), Klimov (1983) given by

$$\frac{S_T}{S_L} = 3.5 \left(\frac{u'}{S_L} \right)^{0.7} \quad (9)$$

which works well for large u'/S_L values are used to obtain approximate values of turbulent flame speed in Table 2. The acoustic time scale can be ignored since the length scale of interest (fuel nozzle to flame) is small compared to the acoustic wavelength and the speed of sound is large compared to convective velocities. The frequency of the fundamental mode is $f_1 \propto \tau^{-1}$ and therefore $f_{1\text{H0}} < f_{1\text{H20}}$. The trend of increase in frequency due to addition of hydrogen is consistent with the experiment and the phenomenological model discussed above shows the right trends as shown in Table 2. It is important to note that the convective and consumption processes happen simultaneously and therefore some overlap in these time scales can be expected. Also, these time scales are dependent delays caused by local unmixedness which as seen from Figs. 16 and 17 are quite different. Therefore, some differences are can be expected. The overestimation of the frequencies in LES is attributed to the adiabatic walls, which slightly underestimate l because of the larger extent of flashback. It is important to note that lift-off events add an additional time scale to τ , which further reduces the frequency of H0 compared to H20. Heat loss close to the wall (in experiments) reduces flashback tendency due to lower local reaction rates and increases the likelihood of lift-off events (Massey et al. 2021, 2022) which explains the overestimation of the frequencies in LES.

The shift of the flame upstream can be correlated with the extinction strain rate, bulk mean velocity and laminar flame speed (s_L) as $l \sim (U_b - s_L)/\kappa_{\text{ext}}$. This correlation is obviously not comprehensive and additional effects (local mixing, thermoacoustic amplitude, diffusivity, etc.) discussed above are ignored for simplicity. As extinction strain rate, laminar flame speed and consumption speed increase with H_2 addition, it is expected that the

fundamental frequency will increase with hydrogen blending based on the above arguments, as shown in Fig. 25 in the Appendix. Note that all cases operate at the same thermal power ($P_{\text{kW}} = 20 \text{ kW}$), and thus Helmholtz acoustics cannot explain the increase in frequency alone. However, the flame cannot shift upstream indefinitely due to the high velocity further upstream in the nozzle. Therefore, it is expected that the decrease in consumption time scale (τ_c) rather than convective time scale ($\tau_{\text{conv}} \approx l/U_b$) contributes more to the increase in frequency at higher H_2 levels. Additional cases (at $P_{\text{th}} = 20 \text{ kW}$ and $\phi = 0.65$) with higher hydrogen blending used to demonstrate the increase in frequency in “Appendix 1” are not discussed further in this work.

It should be noted that the time delays vary with time and that the length l is only weakly defined to draw a conceptual understanding. Additionally, the flame is not a compact element with respect to convective perturbations, making it difficult to define a unique and meaningful length scale. However, the upstream shift in the flame is apparent from Fig. 11a and b, which is sufficient to gather a qualitative understanding of the convective time scale. The response of the flame also changes with hydrogen addition, and additional convective scaling (Ghani and Polifke 2021) feature in such cases. Furthermore, there are additional driving mechanisms in this complex configuration with their own time scales, such as flame-vortex coupling (see Figs. 4 and 5 in the “Appendix”) and their discussion is beyond the scope of the present work. But the above conceptual arguments are sufficient to qualitatively understand the increase in the fundamental frequency with hydrogen addition.

4.4 Coherent Flow Structures

Figures 26 and 27 demonstrate the flame-flow interaction by displaying the flame’s temporal evolution and streamlines. The figures illustrate various vortical structures on the inner and outer shear layers, which interact with the flame. The streamlines also feature a recirculation zone that constitutes the vortex breakdown bubble. This coherent flow structure is crucial in determining flame stabilization. In case H0, Fig. 4 shows two vortex breakdown bubbles in the combustor, with the upstream bubble being asymmetric. The asymmetry is likely due to intermittently occurring helical instabilities that have been observed in experiments for the same case (Datta et al. 2022). The characteristics of the VBB, its asymmetry, and the associated helical instabilities are presented in the following discussion.

Vortex breakdown is a phenomenon that occurs when the cross-sectional area of a vortex suddenly increases, resulting in a low pressure and reverse flow region. This phenomenon is typically caused by an adverse pressure gradient encountered by the vortex core (Lucca-Negro and O’doherly 2001). The VBB can be identified by the V-shaped contour lines near the dump plane (see Figs. 28 and 29 in “Appendix 1”) and are clearly visible during instants t_1 to t_4 . The normalised phase-averaged gauge pressure given by $(p^* - p_\infty)/p_\infty$, where p^* denotes the phase-averaged pressure and p_∞ denotes the ambient pressure, is shown in Fig. 18. The phase-averaged pressure at a particular instant is computed by averaging across several samples separated by the respective thermoacoustic phase difference of 2π . Strong pressure fluctuations in the combustor can modulate the VBB, as observed in Figs. 28 and 29. Figure 18a illustrates the radial pressure variation, which reveals an asymmetry within the VBB, providing a plausible explanation for the asymmetrical VBB observed in case H0. On the other hand, in case H20, the VBB is more or less symmetric in the H20 case, which is consistent with the symmetry observed in Fig. 5. The presence of a strong helical instability is suggested by the asymmetry observed in case H0. Past studies showed a correlation between swirl number and the presence of helical instabilities

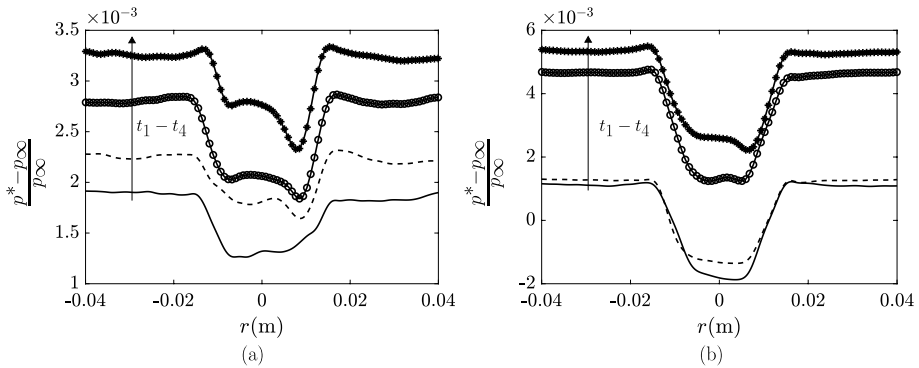


Fig. 18 Radial variation of phase-averaged gauge pressure normalised by ambient pressure for case **a** H0 and **b** H20 at $z = 0$ m

(Gupta et al. 1984; Syred 2006; Manoharan et al. 2020; Fredrich et al. 2021a; Liang and Maxworthy 2005). Thus, studying the swirl number and its fluctuations in the combustor is of interest.

The swirl number S_1 is defined as the ratio of axial flux of azimuthal momentum and axial flux of axial momentum (Gupta et al. 1984; Candel et al. 2014) and is given by,

$$S_1 = \frac{\int_0^R \rho U_z U_\theta r^2 dr}{R \int_0^R [\rho U_z^2 + (p - p_\infty)] r dr}, \tag{10}$$

where R is the duct radius which varies with axial location, ρ is the fluid density, U_z is the axial velocity, U_θ is the tangential or circumferential velocity, p is the static pressure and p_∞ is the ambient pressure. The duct radius is equal to the nozzle radius at the dump-plane and the maximum width of the combustor at $z = 60$ mm. An alternative definition of swirl number (Beer and Chigier 1972) is given by

$$S_2 = \frac{\int_0^R \rho U_z U_\theta r^2 dr}{R \int_0^R \rho U_z^2 r dr}. \tag{11}$$

However, it was shown recently (Vignat et al. 2022) that the pressure term is important to conserve axial flux of axial momentum especially close to regions of area change. Also, the presence of significant thermoacoustic oscillation necessitates the use of the pressure term. Since the region of interest is the nozzle exit, the pressure term is not neglected.

Figure 19a displays the fluctuations in swirl number at the $z = 0$ mm. The non-reacting case shows a fairly stable (not intermittent) PVC (not shown) as indicated by its larger mean swirl number S_1 and fluctuations that are an order of magnitude lower compared to H0 and H20. The oscillations in swirl number S_1 for H0 and H20 primarily stem from thermoacoustic oscillations, helical instabilities and turbulence. In comparison to H20, H0 has a higher time-averaged swirl number (S_1), and its fluctuations are also greater at $z = 0$ mm as shown in Table 3. The mean and fluctuations are much lower for both cases (H0 and H20) at $z = 60$ mm as indicated in Table 3 and the swirl number variation for this location is shown in Fig. 19b. The importance of considering thermoacoustic pressure oscillations can be seen from the fairly similar values of S_2 at $z = 0$ mm which would be insufficient

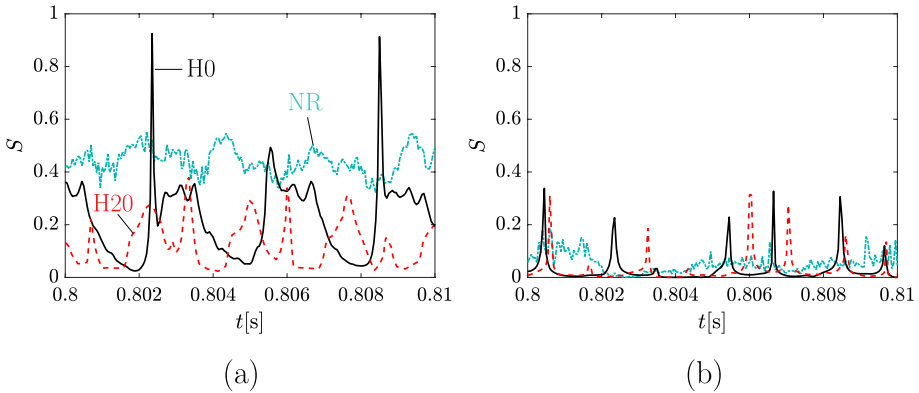


Fig. 19 Swirl number fluctuations at **a** $z = 0$ mm and **b** $z = 60$ mm planes for the two cases along with the non-reacting (NR) case

Table 3 Time-averaged and variance of swirl numbers for different cases

Case	z (mm)	$\langle S_1 \rangle$	$\langle S_1^2 \rangle$	$\langle S_2 \rangle$	$\langle S_2^2 \rangle$
NR	0	0.42	0.003	0.49	0.004
H0	0	0.21	0.058	0.43	0.009
H20	0	0.14	0.015	0.44	0.050
NR	60	0.075	0.003	0.40	0.054
H0	60	0.025	0.003	0.28	0.046
H20	60	0.023	0.002	0.30	0.031

in explaining the absence of a steady PVC in the reacting cases. It is worth noting that H0 exhibits intermittent spikes of very high swirl number values. A recent study (Manoharan et al. 2020) has revealed that beyond a critical value, the swirl number leads to the excitation of helical instabilities via the precession of the vortex breakdown bubble. The higher level of fluctuations and the intermittent spikes in swirl number are the source of intermittent helical instabilities, which result in the asymmetry observed in the upstream vortex breakdown bubble for H0. Zhang et al. (2023) showed that the transient dynamics of the helical instability depends on the competition between convection, production and viscous diffusion of velocity perturbations. Since swirl number is derived from velocity, findings of Zhang et. al. can be related with the intermittency in swirl number. However, it should be noted that the study by Zhang et al. (2023) considered premixed flames without a dominant thermoacoustic oscillation, which are different from the conditions in the current study.

It is interesting to analyse the flame and flow field during the thermoacoustic cycle in a plane perpendicular to the streamwise direction. Figure 20 displays the streamlines along with the reaction rate on an $x - y$ plane at $z = 0.025$ m. The overlaid reaction rate contours show two nearly concentric circular flames associated with the inner and outer shear layers. The streamlines within the inner flame zone correspond to the flow within the IRZ and reveal both a swirling and radial motion. The consequence of the swirl number fluctuation can be clearly seen in the streamline pattern. The swirling motion is dominant in the IRZ during instant t_8 to t_3 when the inner and outer flames are distinctly separated.

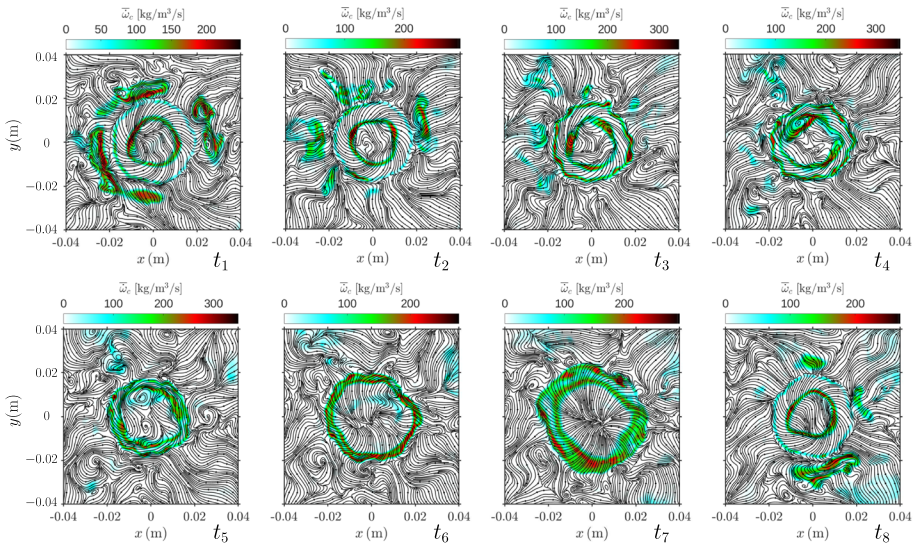


Fig. 20 Evolution of local reaction rates and streamlines in $z = 0.025$ m plane for case H0

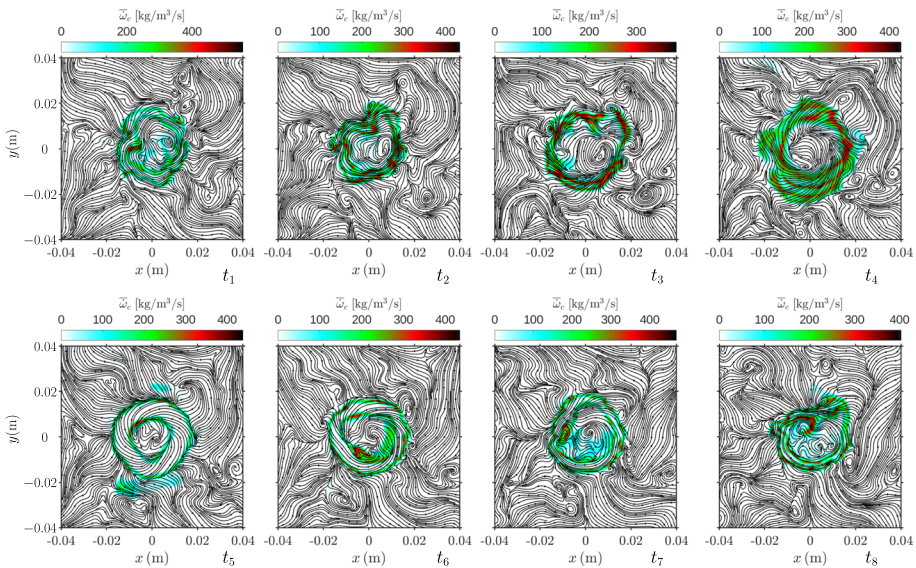


Fig. 21 Evolution of local reaction rates and streamlines in $z = 0.025$ m plane for case H20

During instants t_4 to t_7 , the radial motion in the IRZ is dominant during which inner and outer flames are closer to each other. The switching between swirling and radial motion is a result of the swirl number fluctuations and this results in the flame flapping seen in Fig. 16. Flame flapping motion is a characteristic feature of swirl stabilised flames with swirl number fluctuations (Candel et al. 2014; Palies et al. 2010). At certain instants, such as t_3 , t_4 and t_5 dominant vortical motion can also be discerned in the IRZ which perturb the

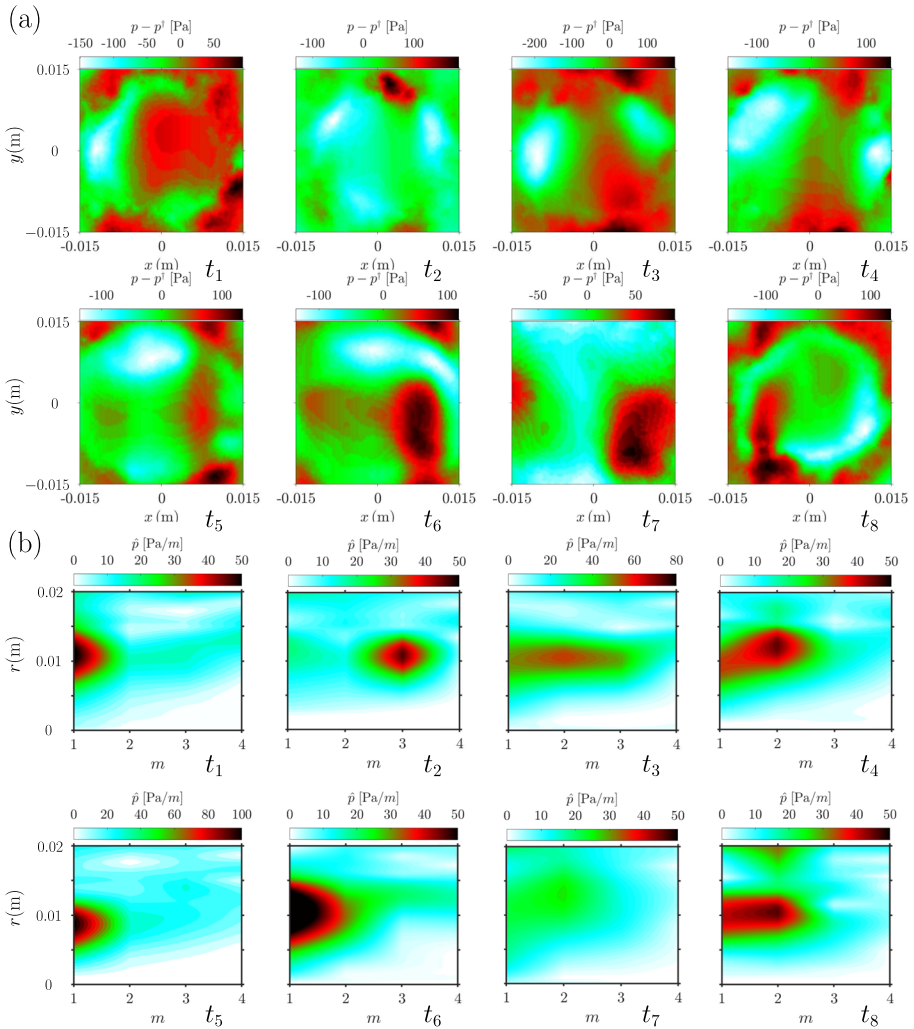


Fig. 22 Evolution of $p - p^\dagger$, where p^\dagger is the surface averaged pressure in $z = 0.025$ m plane and the azimuthally Fourier transformed pressure for case H0

flame surface significantly. The streamlines in case H20 shown in Fig. 21 reveal rarely any instant that has a dominant radial motion like case H0 at instant t_7 . The streamlines show a swirling nature within the IRZ for almost all instants and this is expected since the swirl number fluctuations are lower. The streamlines are also much more incoherent in this case compared to case H20.

Helical structure in swirling flows features low pressure cores and are often recognised using pressure contours. Therefore, it is interesting to analyse the pressure in the $x - y$ plane before looking at their three-dimensional structures. Figure 22a shows the contours of the difference in the pressure and surface averaged pressure, p^\dagger . These contours reveal several low pressure zones which change in both number and strength. Figure 22b shows the azimuthally Fourier transformed pressure given by the Discrete Fourier Transform

(DFT) $2\pi\hat{p} = \sum_{i=0}^N (p - p^\dagger)(r, \theta_i) e^{-im\theta_i}$, where m is the azimuthal wavenumber, $\theta_i = 2\pi i/N$ is the azimuth and N is total number azimuthal points. It should be noted that the presence of a non-zero amplitude at an arbitrary wavenumber may not always necessarily indicate the presence of a coherent structure since the helical modes are very weak and of similar order of magnitude as the background turbulence. Therefore, these plots are interpreted in conjunction with the pressure contour, streamlines and the 3D structures shown next.

These contours show that there is switching between azimuthal wavenumbers during the thermoacoustic oscillation. For instance, at instant t_1 a large low pressure region is visible in Fig. 22 which corresponds to $m = 1$. Figure 20 indicates a streamline pattern that resembles a the superposition of a source and vortex flow (swirling and radially outward flow) in this region accompanied by a local increase in reaction rate. The 3D structures shown in Fig. 24 that are represented by pressure iso-contours reveal that this is indeed a manifestation of a $m = 1$ helical mode. This structure then breaks down into three low pressure zones seen in Fig. 22a which correspond to $m = 3$ as shown in Figs. 22b and 24. This structure does not modulate the flow field significantly and only a small change in curvature can be discerned amidst the background swirling flow. Mode merging is seen in the next instant when $m = 2$ mode appears and persists until t_4 . The vortical motion resulting from this mode is visible in Fig. 20 and the corresponding double helix structure is shown in Fig. 24. The rest of the cycle is dominated by either a single helix or $m = 0$ mode which results in a incoherent pressure contour like at instant t_7 . Note that a non-axisymmetric VBB may also result in a $m = 1$ mode because the DFT is performed along concentric circles. In contrast to case H0, which features higher wavenumbers, case H20 dominantly features $m = 1$ modes (see Fig. 23b) which are most likely the result of slight asymmetry in VBB as also seen in Fig. 18b. During time instants t_1, t_6 and t_7 , small contributions at $m > 1$ are visible in the Fourier transformed pressure, but distinct low pressure regions are not discernible. At t_6 , the pressure contours in Fig. 23a reveal that there is two low pressure zones and a third zone of high pressure in the IRZ. Since DFT does not distinguish between positive and negative values of $p - p^\dagger$, $m = 3$ can be disregarded at this instant as the third zone does not correspond to a low pressure zone. All other instants at which $m > 1$ appears corresponds to weak and incoherent zones which do not reveal a coherent 3D structure as shown in Fig. 24.

In Fig. 24, a range of coherent structures can be observed, which are represented by pressure isosurfaces. Different helical coherent structures are denoted using the azimuthal wavenumber m which is considered to be positive for structures which are counter-winding as suggested by Liang and Maxworthy (2005). At instant t_1 , the pressure isosurface representing the vortex core converges towards the centre cone tip and begins to precess as it enters the combustion chamber. It is important to note that the precession and swirl direction of the vortex core are the same, as indicated by the red arrow in Fig. 24 at time t_1 . The resulting structure takes the form of a single helix with a wavenumber $m = +1$ because it is counter-winding. Additionally, a toroidal vortex ($m = 0$) is visible which is shed from the outer shear layer. This corresponds to the twin vortex structure shown in Figs. 26 and 27 and has been reported in a previous study (Fredrich et al. 2021b). The toroidal vortex is shed due to the pulsating axial velocities in the nozzle during thermoacoustic oscillations.

At instant t_2 , the single helix weakens, and a triple helical structure emerges, along with a toroidal vortex. This triple helical structure corresponds to the vortex roll-ups on the inner shear layer, as depicted in Fig. 26. At time t_3 , the red pressure isosurface has a slightly higher value than the blue isosurface, indicating a single helical structure further downstream. Within the red isosurface, the blue isosurface shows a double helical

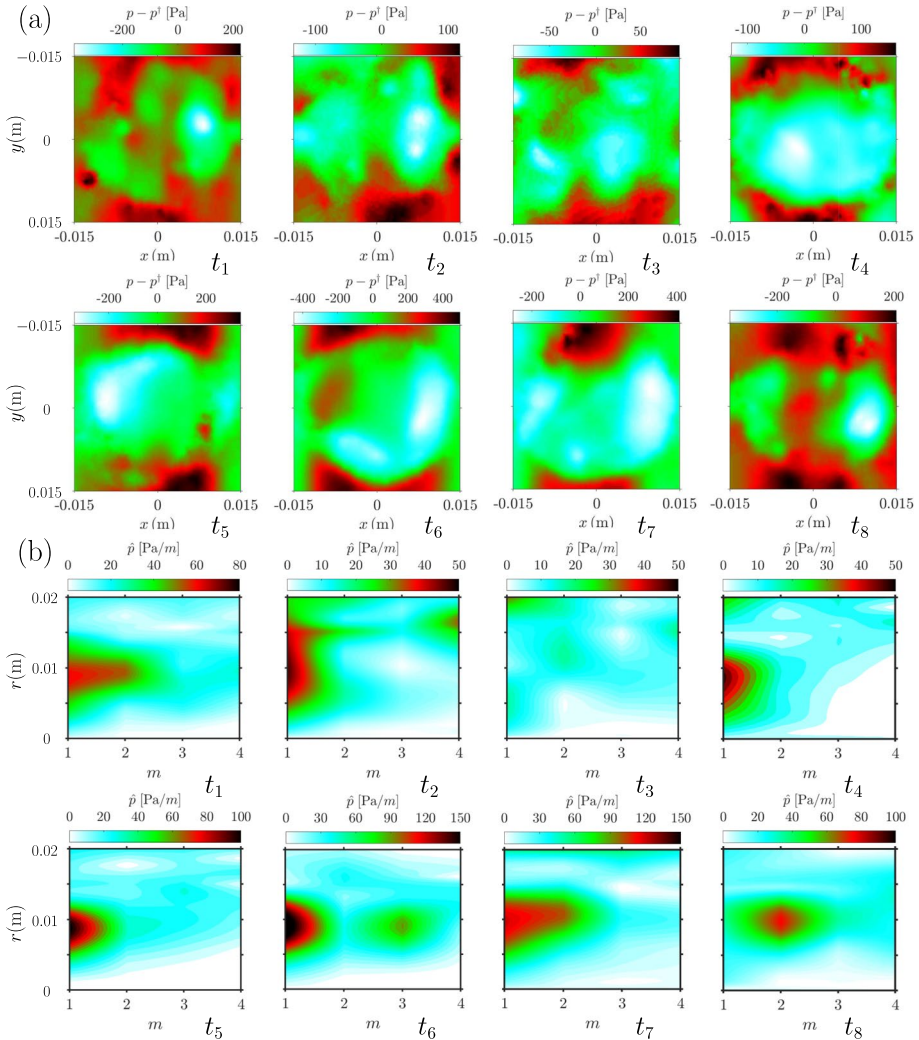


Fig. 23 Evolution of $p - p^\dagger$, where p^\dagger is the surface averaged pressure in $z = 0.025$ m plane and the azimuthally Fourier transformed pressure for case H20

structure. These helical structures appear intermittently and are short-lived. At time t_7 , as the pressure in the combustion chamber starts to decrease, only the VBB is visible. Among structures with non-zero wavenumbers, the single helical structure ($m = +1$) has the highest strength and its intermittent occurrence results in the asymmetric VBB structure in the averaged flow field. The addition of hydrogen mostly dampens the non-zero wavenumbers as shown at t_1 in Fig. 24b, consistent with the experimental study (Datta et al. 2022). Structures with $m > 1$ are rare in case H20 and usually very incoherent as at instants t_3 and t_8 in Fig. 24b. Since the amplitude of the pressure fluctuations induced by the helical instabilities is 1–2 orders of magnitude lower than the thermoacoustic oscillation, it is not expected that the helical instabilities influence the thermoacoustic behaviour as much as vice-versa.

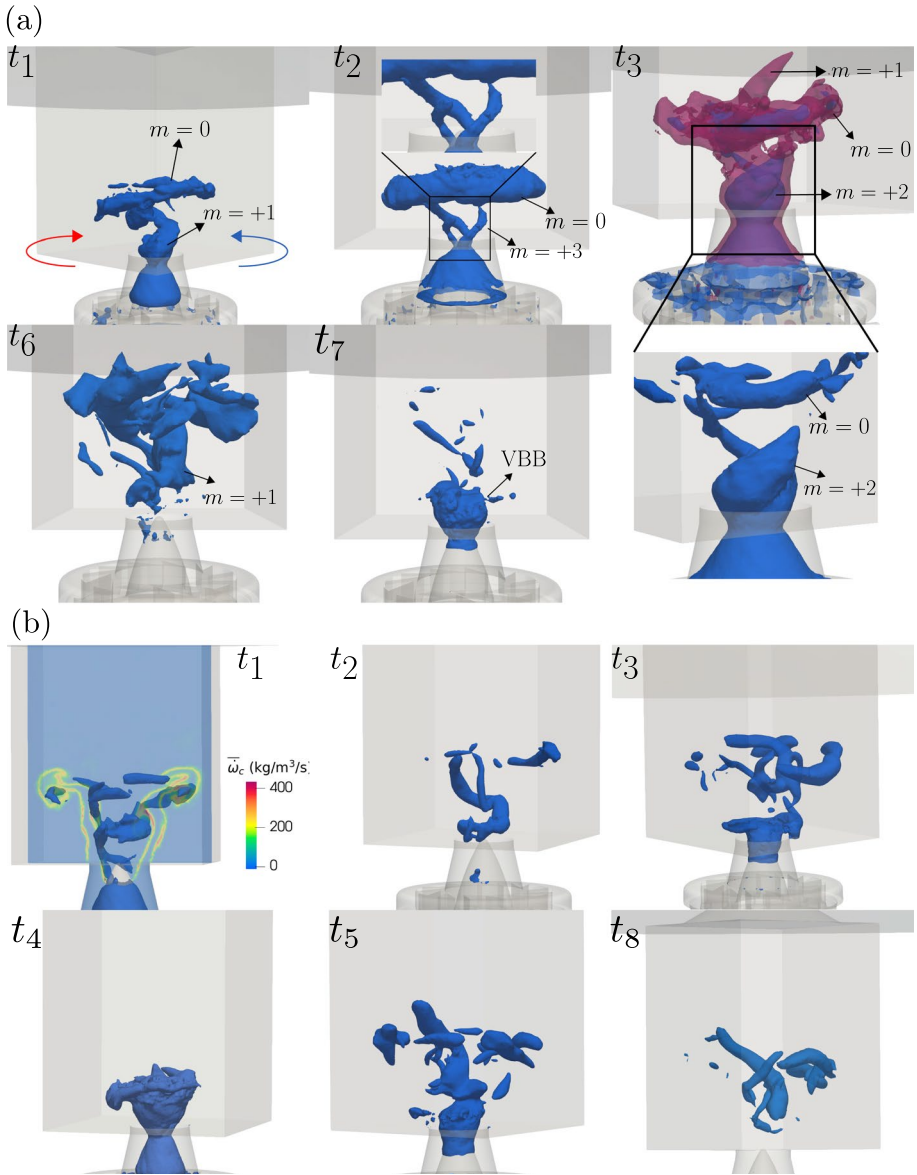


Fig. 24 Three dimensional coherent structures visualised using isosurfaces of pressure for case **a** H0 and **b** H20. The red and blue arrows indicate the precession (and swirl) and winding directions, respectively

The selection of higher wavenumbers ($m > 1$) in swirling flow involves complex dynamics (Liang and Maxworthy 2005; Gallaire and Chomaz 2003a, b; Douglas et al. 2021) that are beyond the scope of this work. Various physical mechanisms, including axial shear, inertial waves due to coriolis forces, azimuthal shear, and centrifugal instabilities, are at play in swirling flow. A dominant thermoacoustic oscillation is also at

play in conjunction with these instabilities which makes this challenging to address and is the topic of a future work.

5 Conclusions

The effects of hydrogen addition on combustion dynamics in the PRECCINSTA burner are studied using large eddy simulation. Two atmospheric cases are explored under lean conditions: one with a CH₄-air mixture and the other with a blended fuel H₂-CH₄ (20–80% by volume) and air mixture. An unstrained flamelet model is utilised for sub-grid scale combustion closure. The simulation results are validated using measured statistics for velocity, and the overall agreement is satisfactory.

The simulations capture the shift from period-1 to period-2 dynamics upon addition of H₂, which is attributed to modal interactions between the plenum and chamber acoustic modes. Quantitative comparisons of thermoacoustic features are discussed and the amplitudes and frequencies are overestimated in the LES. The overestimation in amplitudes is linked to the lack of damping in the simulation, similar to previous studies. The overestimation in frequencies is associated with the use of adiabatic walls, resulting in a quicker response of the flames due to flashback. However, the lack of temperature measurements calls for advanced thermal treatments at walls which are beyond the scope of the present work.

The two cases exhibit a similar thermoacoustic feedback loop that is driven by mixture fraction perturbations produced by the pressure fluctuations in the combustor. However, when a small volume fraction of hydrogen is added, there is a significant change in the system's dynamics. The addition of hydrogen results in two notable changes in the thermoacoustic behavior. Firstly, the amplitude of thermoacoustic oscillation nearly doubles with the addition of 20% H₂ by volume due to higher mixture fraction fluctuations in the nozzle. Secondly, the system transitions from period-1 LCO to period-2 LCO, which is associated with modal interactions between the plenum and chamber mode.

The pure methane case displayed intermittent hydrodynamic instabilities, which were significantly influenced by thermoacoustic oscillation. The presence of the intermittent helical instability was confirmed using the radial pressure variation and swirl number fluctuations. Both cases exhibited axisymmetric toroidal vortex shedding due to large amplitude pressure oscillations. However, the case with H₂ showed a more symmetric flow field due to weaker swirl number fluctuations. In the absence of hydrogen, co-rotating and counter-winding helical instabilities with azimuthal wavenumbers of $m = +1, +2$ and $+3$ were observed. These instabilities evolved intermittently and were mostly suppressed with the addition of hydrogen. The mode selection characteristics of these helical instabilities will be examined in a future study.

Appendix 1

See the Figs. 25, 26, 27, 28 and 29.

Fig. 25 Fundamental frequency variation with hydrogen addition for 4 cases. Cases H40 and H50 represent 40% and 50 % hydrogen blending by volume which are reported in Table 1 Ref. Kushwaha et al. (2021)

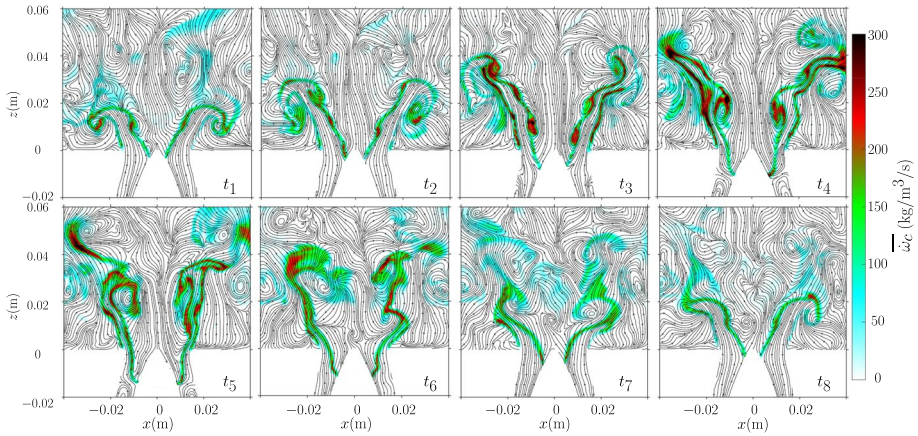
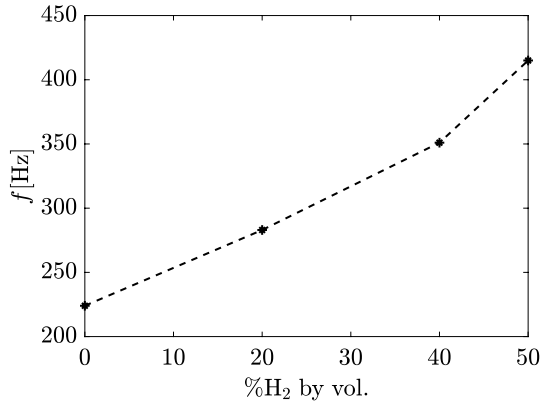


Fig. 26 Temporal evolution of the local reaction rate contours and streamlines in midplane normal to y-axis for case H0 during one cycle of the fundamental mode

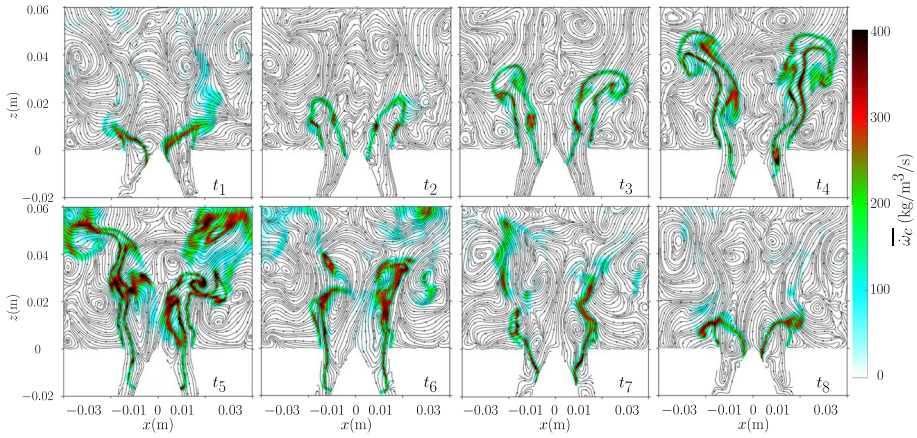


Fig. 27 Temporal evolution of the local reaction rate contours and streamlines in midplane normal to y-axis for case H20 during one cycle of the fundamental mode

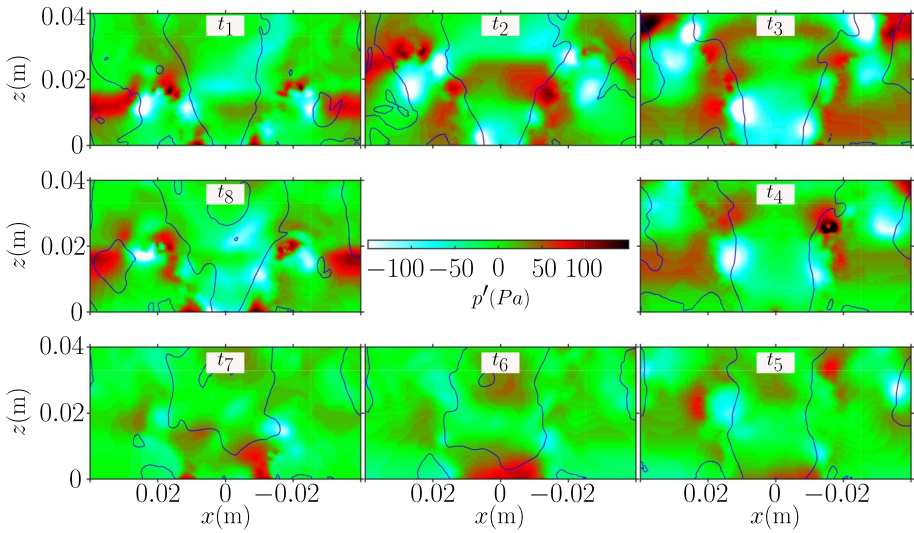


Fig. 28 Temporal evolution of the fluctuating pressure contours in the midplane normal to y-axis for case H0 during one cycle of the fundamental mode. Dark blue line is the zero axial velocity contour

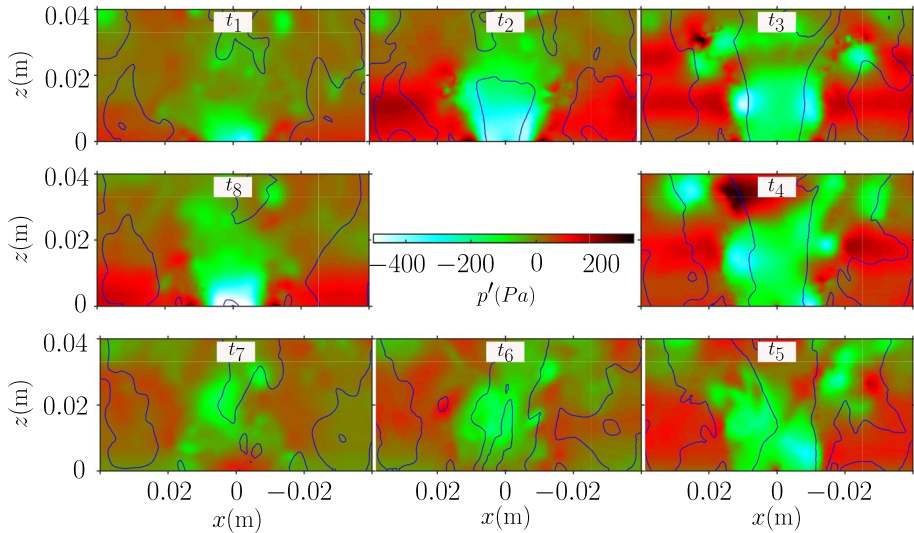


Fig. 29 Temporal evolution of the fluctuating pressure contours in the midplane normal to y -axis for case H20 during one cycle of the fundamental mode. Dark blue line is the zero axial velocity contour

Acknowledgements A. D. Kumar acknowledges the financial support from the Cambridge Trust. The University of Cambridge authors acknowledge the support from Mitsubishi Heavy Industries, Ltd., Japan. This work used the ARCHER2 UK National Supercomputing Service (<https://www.archer2.ac.uk>). The authors are grateful to the EPSRC (Grant number EP/R029369/1) and ARCHER2 for financial and computational support as a part of their funding to the UK Consortium on Turbulent Reacting Flows (<https://www.ukctrf.com>). This project received funding from the European Research Council (ERC) under the European Union's Horizon 2020 research and innovation programme (Grant agreement No. 682383).

Author Contributions ADK performed the simulations with assistance from JCM. IB performed the experiments. NS was responsible for supervision and acquiring funding for Cambridge authors. Cambridge authors conceptualised the work. ADK wrote the original draft and all authors contributed to reviewing and editing the manuscript.

Funding The work reported in this paper was funded by the Cambridge Trust, Mitsubishi Heavy Industries, Engineering and Physical Sciences Research Council and European Research Council.

Declarations

Conflict of interest The authors declare that they have no conflict of interest with this work.

Ethical Approval The authors confirm that they have upheld the integrity of the scientific record, thereby complying with the journal's ethics policy.

Informed Consent The authors confirm that all of the material is owned by them and/or no permissions from third parties are required.

Open Access This article is licensed under a Creative Commons Attribution 4.0 International License, which permits use, sharing, adaptation, distribution and reproduction in any medium or format, as long as you give appropriate credit to the original author(s) and the source, provide a link to the Creative Commons licence, and indicate if changes were made. The images or other third party material in this article are included in the article's Creative Commons licence, unless indicated otherwise in a credit line to the material. If material is not included in the article's Creative Commons licence and your intended use is not

permitted by statutory regulation or exceeds the permitted use, you will need to obtain permission directly from the copyright holder. To view a copy of this licence, visit <http://creativecommons.org/licenses/by/4.0/>.

References

- Agostinelli, P., Laera, D., Chterev, I., Boxx, I., Gicquel, L., Poinso, T.: On the impact of H₂-enrichment on flame structure and combustion dynamics of a lean partially-premixed turbulent swirling flame. *Combust. Flame* **241**, 112120 (2022)
- Aniello, A., Laera, D., Marragou, S., Magnes, H., Selle, L., Schuller, T., Poinso, T.: Experimental and numerical investigation of two flame stabilization regimes observed in a dual swirl H₂-air coaxial injector. *Combust. Flame* **249**, 112595 (2023)
- Beer, J.M., Chigier, N.A.: *Combustion Aerodynamics*. Wiley, New York (1972)
- Beita, J., Talibi, M., Sadasivuni, S., Balachandran, R.: Thermoacoustic instability considerations for high hydrogen combustion in lean premixed gas turbine combustors: a review. *Hydrogen* **2**(1), 33–57 (2021)
- Bénard, P., Lartigue, G., Moureau, V., Mercier, R.: Large-eddy simulation of the lean-premixed preccinsta burner with wall heat loss. *Proc. Combust. Inst.* **37**(4), 5233–5243 (2019)
- Bilger, R.W.: The structure of turbulent nonpremixed flames. *Proc. Combust. Inst.* **22**(1), 475–488 (1989)
- Candel, S., Durox, D., Schuller, T., Bourgo, J.-F., Moeck, J.P.: Dynamics of swirling flames. *Annu. Rev. Fluid Mech.* **46**, 147–173 (2014)
- Chen, Z.X., Swaminathan, N.: Influence of fuel plenum on thermoacoustic oscillations inside a swirl combustor. *Fuel* **275**, 117868 (2020)
- Chen, Z., Ruan, S., Swaminathan, N.: Large eddy simulation of flame edge evolution in a spark-ignited methane-air jet. *Proc. Combust. Inst.* **36**(2), 1645–1652 (2017)
- Chen, Z.X., Langella, I., Swaminathan, N., Stöhr, M., Meier, W., Kolla, H.: Large eddy simulation of a dual swirl gas turbine combustor: flame/flow structures and stabilisation under thermoacoustically stable and unstable conditions. *Combust. Flame* **203**, 279–300 (2019)
- Chen, Z.X., Swaminathan, N., Stöhr, M., Meier, W.: Interaction between self-excited oscillations and fuel-air mixing in a dual swirl combustor. *Proc. Combust. Inst.* **37**(2), 2325–2333 (2019)
- Chen, Z.X., Langella, I., Barlow, R.S., Swaminathan, N.: Prediction of local extinctions in piloted jet flames with inhomogeneous inlets using unstrained flamelets. *Combust. Flame* **212**, 415–432 (2020)
- Chterev, I., Boxx, I.: Flame topology and combustion instability limits of lean premixed hydrogen enriched flames. In: *Proceedings of the 27th International Colloquium on the Dynamics of Explosions and Reactive Systems (ICDERS)*, Beijing, China, vol. 28 (2019)
- Chterev, I., Boxx, I.: Effect of hydrogen enrichment on the dynamics of a lean technically premixed elevated pressure flame. *Combust. Flame* **225**, 149–159 (2021)
- Datta, A., Gupta, S., Chterev, I., Boxx, I., Hemchandra, S.: Impact of hydrogen addition on the thermoacoustic instability and precessing vortex core dynamics in a CH₄/H₂/air technically premixed combustor. *J. Eng. Gas Turb. Power* **144**(2) (2022)
- Dem, C., Stöhr, M., Arndt, C.M., Steinberg, A.M., Meier, W.: Experimental study of turbulence-chemistry interactions in perfectly and partially premixed confined swirl flames. *Z. Phys. Chem.* **229**(4), 569–595 (2015)
- Douglas, C.M., Emerson, B.L., Lieuwen, T.C.: Nonlinear dynamics of fully developed swirling jets. *J. Fluid Mech.* **924** (2021)
- Dowling, A., Hubbard, S.: Instability in lean premixed combustors. *Proc. Inst. Mech. Eng. A J. Power Energy* **214**(4), 317–332 (2000)
- Ducruix, S., Schuller, T., Durox, D., Candel, S.: Combustion dynamics and instabilities: elementary coupling and driving mechanisms. *J. Propuls. Power.* **19**(5), 722–734 (2003)
- Dunstan, T.D., Minamoto, Y., Chakraborty, N., Swaminathan, N.: Scalar dissipation rate modelling for large eddy simulation of turbulent premixed flames. *Proc. Combust. Inst.* **34**(1), 1193–1201 (2013)
- Fiorina, B., Baron, R., Gicquel, O., Thevenin, D., Carpentier, S., Darabiha, N.: Modelling non-adiabatic partially premixed flames using flame-prolongation of ILDM. *Combust. Theory Model.* **7**(3), 449–470 (2003)
- Franzelli, B., Riber, E., Gicquel, L.Y., Poinso, T.: Large eddy simulation of combustion instabilities in a lean partially premixed swirled flame. *Combust. Flame* **159**(2), 621–637 (2012)
- Fredrich, D., Jones, W., Marquis, A.J.: The stochastic fields method applied to a partially premixed swirl flame with wall heat transfer. *Combust. Flame* **205**, 446–456 (2019)

- Fredrich, D., Jones, W.P., Marquis, A.J.: Thermo-acoustic instabilities in the PRECCINSTA combustor investigated using a compressible LES-PDF approach. *Flow Turbul. Combust.* **106**(4), 1399–1415 (2021)
- Fredrich, D., Jones, W., Marquis, A.: A combined oscillation cycle involving self-excited thermo-acoustic and hydrodynamic instability mechanisms. *Phys. Fluids* **33**(8), 085122 (2021)
- Gallaire, F., Chomaz, J.-M.: Mode selection in swirling jet experiments: a linear stability analysis. *J. Fluid Mech.* **494**, 223–253 (2003)
- Gallaire, F., Chomaz, J.-M.: Instability mechanisms in swirling flows. *Phys. Fluids* **15**(9), 2622–2639 (2003)
- Garcia, A.M., Le Bras, S., Polifke, W.: Effect of hydrogen addition on the consumption speed of lean premixed laminar methane flames exposed to combined strain and heat loss. *Combust. Theory Model.* 1–21 (2023)
- Gauducheau, J., Denet, B., Searby, G.: A numerical study of lean CH_4/H_2 /air premixed flames at high pressure. *Combust. Sci. Technol.* **137**(1–6), 81–99 (1998)
- Germano, M., Piomelli, U., Moin, P., Cabot, W.H.: A dynamic subgrid-scale eddy viscosity model. *Phys. Fluids A* **3**, 1760–1765 (1991)
- Ghani, A., Polifke, W.: Control of intrinsic thermoacoustic instabilities using hydrogen fuel. *Proc. Combust. Inst.* **38**(4), 6077–6084 (2021)
- Gong, Y.: Applications of a numerical method in study of combustion instabilities. Ph.D. Thesis, Imperial College London (2022)
- Goodwin, D.G., Moffat, H.K., Speth, R.L.: Cantera: an object-oriented software toolkit for chemical kinetics, thermodynamics, and transport processes (2018)
- Gupta, A.K., Lilley, D.G., Syred, N.: Swirl flows. Tunbridge Wells (1984)
- Indlekofer, T., Ahn, B., Kwah, Y.H., Wiseman, S., Mazur, M., Dawson, J.R., Worth, N.A.: The effect of hydrogen addition on the amplitude and harmonic response of azimuthal instabilities in a pressurized annular combustor. *Combust. Flame* **228**, 375–387 (2021)
- Kabiraj, L., Sujith, R.: Nonlinear self-excited thermoacoustic oscillations: intermittency and flame blow-out. *J. Fluid Mech.* **713**, 376–397 (2012)
- Karlis, E., Liu, Y., Hardalupas, Y., Taylor, A.M.K.P.: H_2 enrichment of CH_4 blends in lean premixed gas turbine combustion: an experimental study on effects on flame shape and thermoacoustic oscillation dynamics. *Fuel* **254**, 115524 (2019)
- Karmarkar, A., Gupta, S., Boxx, I., Hemchandra, S., O'Connor, J.: Impact of precessing vortex core dynamics on the thermoacoustic instabilities in a swirl-stabilized combustor. *J. Fluid Mech.* **946**, 36 (2022)
- Klimov, A.: Premixed turbulent flames-interplay of hydrodynamic and chemical phenomena. *Flames Lasers React. Syst.* 133–146 (1983)
- Kolla, H., Rogerson, J., Swaminathan, N.: Validation of a turbulent flame speed model across combustion regimes. *Combust. Sci. Technol.* **182**(3), 284–308 (2010)
- Kraus, C., Selle, L., Poinot, T.: Coupling heat transfer and large eddy simulation for combustion instability prediction in a swirl burner. *Combust. Flame* **191**, 239–251 (2018)
- Kumar, A.D., Massey, J.C., Stöhr, M., Meier, W., Swaminathan, N.: Period-2 thermoacoustics in a swirl-stabilised partially premixed flame computed using large eddy simulation. *Flow Turbul. Combust.* (2023) (Accepted)
- Kushwaha, A., Kasthuri, P., Pawar, S.A., Sujith, R.I., Chterev, I., Boxx, I.: Dynamical characterization of thermoacoustic oscillations in a hydrogen-enriched partially premixed swirl-stabilized methane/air combustor. *J. Eng. Gas Turb. Power* **143**(12) (2021)
- Kushwaha, A., Kasthuri, P., Pawar, S.A., Sujith, R., Chterev, I., Boxx, I.: Erratum: “dynamical characterization of thermoacoustic oscillations in a hydrogen-enriched partially premixed swirl-stabilized methane/air combustor” [*ASME J. Eng. Gas Turbines Power* **143**(12), 121022. *J. Eng. Gas Turb. Power* 1–4 (2023)] (2023)
- Langella, I., Chen, Z.X., Swaminathan, N., Sadasivuni, S.K.: Large-eddy simulation of reacting flows in industrial gas turbine combustor. *J. Propul. Power* **34**(5), 1269–1284 (2018)
- Langella, I., Heinze, J., Behrendt, T., Voigt, L., Swaminathan, N., Zedda, M.: Turbulent flame shape switching at conditions relevant for gas turbines. *J. Eng. Gas Turbine Power* **142**(1), 011026 (2020)
- Lee, M.C., Yoon, J., Joo, S., Kim, J., Hwang, J., Yoon, Y.: Investigation into the cause of high multi-mode combustion instability of $\text{H}_2/\text{CO}/\text{CH}_4$ syngas in a partially premixed gas turbine model combustor. *Proc. Combust. Inst.* **35**(3), 3263–3271 (2015)
- Liang, H., Maxworthy, T.: An experimental investigation of swirling jets. *J. Fluid Mech.* **525**, 115–159 (2005)
- Lieuwen, T., Zinn, B.T.: The role of equivalence ratio oscillations in driving combustion instabilities in low NO_x gas turbines. *Proc. Combust. Inst.* **27**(1), 1809–1816 (1998)

- Lilly, D.K.: A proposed modification of the germano subgrid-scale closure method. *Phys. Fluids A: Fluid Dyn.* **4**(3), 633–635 (1992)
- Lourier, J.-M., Stöhr, M., Noll, B., Werner, S., Fiolitakis, A.: Scale adaptive simulation of a thermoacoustic instability in a partially premixed lean swirl combustor. *Combust. Flame* **183**, 343–357 (2017)
- Lucca-Negro, O., O’doherly, T.: Vortex breakdown: a review. *Prog. Energy Combust.* **27**(4), 431–481 (2001)
- Manoharan, K., Frederick, M., Clees, S., O’Connor, J., Hemchandra, S.: A weakly nonlinear analysis of the precessing vortex core oscillation in a variable swirl turbulent round jet. *J. Fluid Mech.* **884**, 29 (2020)
- Massey, J.C., Chen, Z.X., Swaminathan, N.: Lean flame root dynamics in a gas turbine model combustor. *Combust. Sci. Technol.* **191**(5–6), 1019–1042 (2019)
- Massey, J.C., Langella, I., Swaminathan, N.: A scaling law for the recirculation zone length behind a bluff body in reacting flows. *J. Fluid Mech.* **875**, 699–724 (2019)
- Massey, J.C., Chen, Z.X., Swaminathan, N.: Modelling heat loss effects in the large eddy simulation of a lean swirl-stabilised flame. *Flow Turbul. Combust.* **106**(4), 1355–1378 (2021)
- Massey, J.C., Chen, Z.X., Stöhr, M., Meier, W., Swaminathan, N.: On the blow-off correlation for swirl-stabilised flames with a precessing vortex core. *Combust. Flame* **239**, 111741 (2022)
- Meier, W., Duan, X.R., Weigand, P.: Investigations of swirl flames in a gas turbine model combustor: II. Turbulence-chemistry interactions. *Combust. Flame* **144**(1–2), 225–236 (2006)
- Meier, W., Weigand, P., Duan, X.R., Giezendanner-Thoben, R.: Detailed characterization of the dynamics of thermoacoustic pulsations in a lean premixed swirl flame. *Combust. Flame* **150**(1–2), 2–26 (2007)
- Nemittallah, M.A., Rashwan, S.S., Mansir, I.B., Abdelhafez, A.A., Habib, M.A.: Review of novel combustion techniques for clean power production in gas turbines. *Energy Fuels* **32**(2), 979–1004 (2018)
- Oberleithner, K., Stöhr, M., Im, S.H., Arndt, C.M., Steinberg, A.M.: Formation and flame-induced suppression of the precessing vortex core in a swirl combustor: experiments and linear stability analysis. *Combust. Flame* **162**(8), 3100–3114 (2015)
- Palies, P., Durox, D., Schuller, T., Candel, S.: The combined dynamics of swirler and turbulent premixed swirling flames. *Combust. Flame* **157**(9), 1698–1717 (2010)
- Pierce, C.D., Moin, P.: A dynamic model for subgrid-scale variance and dissipation rate of a conserved scalar. *Phys. Fluids* **10**(12), 3041–3044 (1998)
- Pope, S.B.: *Turbulent Flows*. Cambridge University Press, Cambridge (2000)
- Rayleigh, L.: On the dynamics of revolving fluids. *Proc. R. Soc. Lond.* **93**(648), 148–154 (1917)
- Ren, J., Qin, W., Egofoopoulos, F., Tsotsis, T.: Strain-rate effects on hydrogen-enhanced lean premixed combustion. *Combust. Flame* **124**(4), 717–720 (2001)
- Roux, S., Lartigue, G., Poinso, T., Meier, U., Bérat, C.: Studies of mean and unsteady flow in a swirled combustor using experiments, acoustic analysis, and large eddy simulations. *Combust. Flame* **141**(1–2), 40–54 (2005)
- Roux, S., Lartigue, G., Poinso, T., Meier, U., Bérat, C.: Studies of mean and unsteady flow in a swirled combustor using experiments, acoustic analysis, and large eddy simulations. *Combust. Flame* **141**(1–2), 40–54 (2005)
- Ruan, S., Swaminathan, N., Darbyshire, O.: Modelling of turbulent lifted jet flames using flamelets: a priori assessment and a posteriori validation. *Combust. Theory Model.* **18**(2), 295–329 (2014)
- Schuller, T., Marragou, S., Oztarlik, G., Poinso, T., Selle, L.: Influence of hydrogen content and injection scheme on the describing function of swirled flames. *Combust. Flame* **240**, 111974 (2022)
- Shanbhogue, S., Sanusi, Y., Taamallah, S., Habib, M., Mokheimer, E., Ghoniem, A.: Flame macrostructures, combustion instability and extinction strain scaling in swirl-stabilized premixed CH₄/H₂ combustion. *Combust. Flame* **163**, 494–507 (2016)
- Spalding, D.B.: A single formula for the “law of the wall”. *J. Appl. Mech-T ASME.* **28**(3), 455–458 (1960)
- Stöhr, M., Yin, Z., Meier, W.: Interaction between velocity fluctuations and equivalence ratio fluctuations during thermoacoustic oscillations in a partially premixed swirl combustor. *Proc. Combust. Inst.* **36**(3), 3907–3915 (2017)
- Syred, N.: A review of oscillation mechanisms and the role of the precessing vortex core (PVC) in swirl combustion systems. *Prog. Energy Combust. Sci.* **32**(2), 93–161 (2006)
- Terhaar, S., Oberleithner, K., Paschereit, C.O.: Key parameters governing the precessing vortex core in reacting flows: an experimental and analytical study. *Proc. Combust. Inst.* **35**(3), 3347–3354 (2015)
- Tuncer, O., Acharya, S., Uhm, J.: Dynamics, NO_x and flashback characteristics of confined premixed hydrogen-enriched methane flames. *Int. J. Hydrog. Energy* **34**(1), 496–506 (2009)
- Vanierschot, M., Percin, M., Van Oudheusden, B.: Double helix vortex breakdown in a turbulent swirling annular jet flow. *Phys. Rev. Fluids.* **3**(3), 034703 (2018)

- Vignat, G., Durox, D., Renaud, A., Lancien, T., Vicquelin, R., Candel, S.: Investigation of transient PVC dynamics in a strongly swirled spray flame using high speed planar laser imaging of SnO₂ microparticles. *Combust. Flame* **225**, 305–319 (2021)
- Vignat, G., Durox, D., Candel, S.: The suitability of different swirl number definitions for describing swirl flows: accurate, common and (over-) simplified formulations. *Prog. Energy Combust. Sci.* **89**, 100969 (2022)
- Weigand, P., Meier, W., Duan, X.R., Stricker, W., Aigner, M.: Investigations of swirl flames in a gas turbine model combustor: I. Flow field, structures, temperature, and species distributions. *Combust. Flame* **144**(1–2), 205–224 (2006)
- Yin, Z., Stöhr, M.: Time–frequency localisation of intermittent dynamics in a bistable turbulent swirl flame. *J. Fluid Mech.* **882**, 30 (2020)
- Yu, G., Law, C.K., Wu, C.K.: Laminar flame speeds of hydrocarbon+ air mixtures with hydrogen addition. *Combust. Flame* **63**(3), 339–347 (1986)
- Yue, M., Lambert, H., Pahon, E., Roche, R., Jemei, S., Hissel, D.: Hydrogen energy systems: a critical review of technologies, applications, trends and challenges. *Renew. Sust. Energy Rev.* **146**, 111180 (2021)
- Zhang, J., Hui, X., An, Q., Steinberg, A.M.: Transient dynamics of the precessing vortex core in an intermittently shape-transitioning swirl flame. *Combust. Flame* **250**, 112652 (2023)

Authors and Affiliations

Ankit D. Kumar¹ · James C. Massey^{1,2} · Isaac Boxx^{3,4} · Nedunchezian Swaminathan¹

✉ Ankit D. Kumar
adk46@cam.ac.uk

James C. Massey
jcm97@cam.ac.uk

Isaac Boxx
boxx@lom.rwth-aachen.de

Nedunchezian Swaminathan
ns341@cam.ac.uk

¹ Department of Engineering, University of Cambridge, Trumpington Street, Cambridge CB2 1PZ, UK

² Robinson College, University of Cambridge, Grange Road, Cambridge CB3 9AN, UK

³ Institute of Combustion Technology, German Aerospace Center (DLR), Pfaffenwaldring 38-40, 70569 Stuttgart, Germany

⁴ Chair of Optical Diagnostics Energy, Chemical and Process Engineering, RWTH Aachen University, 52062 Aachen, Germany